

RESEARCH PAPER



## Hypoxia-induced GPCPD1 depalmitoylation triggers mitophagy via regulating PRKN-mediated ubiquitination of VDAC1

Ying Liu <sup>a</sup>, Hanwen Zhang <sup>a</sup>, Yiwei Liu <sup>a</sup>, Siyue Zhang <sup>a</sup>, Peng Su <sup>b</sup>, Lijuan Wang <sup>c</sup>, Yaming Li <sup>a</sup>, Yiran Liang <sup>a</sup>, Xiaolong Wang <sup>a</sup>, Weijing Zhao <sup>c</sup>, Bing Chen <sup>c</sup>, Dan Luo <sup>c</sup>, Ning Zhang <sup>a</sup>, and Qifeng Yang <sup>a,c,d</sup>

<sup>a</sup>Department of Breast Surgery, General Surgery, Qilu Hospital of Shandong University, Ji'nan, Shandong, China; <sup>b</sup>Department of Pathology, Qilu Hospital of Shandong University, Ji'nan, Shandong, China; <sup>c</sup>Pathology Tissue Bank, Qilu Hospital of Shandong University, Ji'nan, Shandong, China; <sup>d</sup>Research Institute of Breast Cancer, Shandong University, Ji'nan, Shandong, China

### ABSTRACT

Mitophagy, which selectively eliminates the dysfunctional and excess mitochondria by autophagy, is crucial for cellular homeostasis under stresses such as hypoxia. Dysregulation of mitophagy has been increasingly linked to many disorders including neurodegenerative disease and cancer. Triple-negative breast cancer (TNBC), a highly aggressive breast cancer subtype, is reported to be characterized by hypoxia. However, the role of mitophagy in hypoxic TNBC as well as the underlying molecular mechanism is largely unexplored. Here, we identified GPCPD1 (glycerophosphocholine phosphodiesterase 1), a key enzyme in choline metabolism, as an essential mediator in hypoxia-induced mitophagy. Under the hypoxic condition, we found that GPCPD1 was depalmitoylated by LYPLA1, which facilitated the relocating of GPCPD1 to the outer mitochondrial membrane (OMM). Mitochondria-localized GPCPD1 could bind to VDAC1, the substrate for PRKN/PARKIN-dependent ubiquitination, thus interfering with the oligomerization of VDAC1. The increased monomer of VDAC1 provided more anchor sites to recruit PRKN-mediated polyubiquitination, which consequently triggered mitophagy. In addition, we found that GPCPD1-mediated mitophagy exerted a promotive effect on tumor growth and metastasis in TNBC both *in vitro* and *in vivo*. We further determined that GPCPD1 could serve as an independent prognostic indicator in TNBC. In conclusion, our study provides important insights into a mechanistic understanding of hypoxia-induced mitophagy and elucidates that GPCPD1 could act as a potential target for the future development of novel therapy for TNBC patients.

**Abbreviations:** ACTB: actin beta; 5-aza: 5-azacytidine; BNIP3: BCL2 interacting protein 3; BNIP3L: BCL2 interacting protein 3 like; CCCP: carbonyl cyanide m-chlorophenyl hydrazone; ChIP: chromatin immunoprecipitation; co-IP: co-immunoprecipitation; CQ: chloroquine; CsA: cyclosporine; DOX: doxorubicin; FIS1: fission, mitochondrial 1; FUNDC1: FUN14 domain containing 1; GPCPD1: glycerophosphocholine phosphodiesterase 1; HAM: hydroxylamine; HIF1A: hypoxia inducible factor 1 subunit alpha; HRE: hypoxia response element; IF: immunofluorescence; LB: lysis buffer; LC3B/MAP1LC3B: microtubule associated protein 1 light chain 3 beta; LC-MS: liquid chromatography-mass spectrometry; LYPLA1: lysophospholipase 1; LYPLA2: lysophospholipase 2; MDA231: MDA-MB-231; MDA468: MDA-MB-468; MFN1: mitofusin 1; MFN2: mitofusin 2; MKI67: marker of proliferation Ki-67; OCR: oxygen consumption rate; OMM: outer mitochondrial membrane; OS: overall survival; PalmB: palmostatin B; PBS: phosphate-buffered saline; PINK1: PTEN induced kinase 1; PRKN: parkin RBR E3 ubiquitin protein ligase; SDS: sodium dodecyl sulfate; TOMM20: translocase of outer mitochondrial membrane 20; TNBC: triple-negative breast cancer; VBIT-4: VDAC inhibitor; VDAC1: voltage dependent anion channel 1; WT: wild type.

### ARTICLE HISTORY

Received 8 June 2022  
Revised 13 February 2023  
Accepted 15 February 2023





### KEYWORDS

GPCPD1; hypoxia; mitophagy; PRKN; ubiquitination; VDAC1


## Introduction

Hypoxia is a hallmark of solid tumors. Mitophagy, a selective form of autophagy, occurs under hypoxic conditions as an adaptation to maintain oxygen homeostasis [1]. Under hypoxic conditions, mitochondria self-adaptively reduce oxidative phosphorylation and cytochrome c oxidase activity while increasing reactive oxygen species levels [2]. Because of these alterations, mitophagy is triggered to selectively remove unwanted or damaged mitochondria to control both mitochondrial quantity and quality [3]. Increasing evidence

has shown that dysfunctional mitophagy may contribute to various conditions, including cancer, neurodegeneration, cardiovascular disease, and metabolic disorders [4]. To date, both PINK1-PRKN-dependent (ubiquitin-dependent) and PINK1-PRKN-independent (receptor-dependent) pathways have been described. Distinct mechanisms may be activated in response to different mitochondrial stresses [5]. PINK1-PRKN independent mitophagy was reported to be activated in response to hypoxia or mitochondrial oxidative stress [6]. Under hypoxic conditions, BNIP3, BNIP3L, and FUNDC1, located

**CONTACT** Ning Zhang  [ningzhang@sdu.edu.cn](mailto:ningzhang@sdu.edu.cn)  Department of Breast Surgery, Qilu Hospital, Shandong University, Ji'nan, Shandong 250012, China; Qifeng Yang  [qifeng\\_y\\_sdu@163.com](mailto:qifeng_y_sdu@163.com)  Department of Breast Surgery, Qilu Hospital, Shandong University, Ji'nan, Shandong, China

This article has been corrected with minor changes. These changes do not impact the academic content of the article.

 Supplemental data for this article can be accessed online at <https://doi.org/10.1080/15548627.2023.2182482>

in the outer mitochondrial membrane (OMM), are transcriptionally induced by HIF1A (hypoxia inducible factor 1 subunit alpha). They then directly bind to MAP1LC3/LC3 via the LC3-interacting region/LIR motifs and subsequently induce mitophagy [7,8]. In previous studies, PRKN was reported to be upregulated under hypoxic conditions [9]; however, it remains unclear whether and to what extent the ubiquitination-associated PINK1-PRKN pathway participates in the regulation of hypoxia-induced mitophagy. Meanwhile, the role of hypoxia-induced mitophagy in cancer progression remains largely unexplored.

Triple-negative breast cancer (TNBC) lacks the expression of estrogen and progesterone receptors, along with ERBB2/HER2 (erb-b2 receptor tyrosine kinase 2) [10]. Although TNBC constitutes only 10–15% of breast cancers, it accounts for one-third of breast cancer-specific deaths due to the lack of targeted therapies and its highly aggressive behavior [11]. Recent evidence suggests that among the different breast cancer subtypes, TNBC is the most characterized by hypoxia [12,13]. Identifying the underlying molecular mechanisms may assist in the design of innovative therapeutic strategies for TNBC. To investigate the detailed molecular mechanism by which hypoxia triggers mitophagy and how hypoxia-induced mitophagy contributes to TNBC progression, we applied ribonucleic acid (RNA)-seq to screen for genes altered under hypoxic conditions and treatment with carbonyl cyanide m-chlorophenyl hydrazone (CCCP, an uncoupling agent that induces mitophagy) in TNBC cells. After intersection analysis, we identified 18 genes as potential factors mediating hypoxia-induced mitophagy. GPCPD1 (glycerophosphocholine phosphodiesterase 1), a key enzyme in choline metabolism, was identified as a novel regulator of hypoxic mitophagy using an mt-Keima high-content screening system. Here, we report for the first time that the dephosphorylation process of GPCPD1 assists its trafficking to the mitochondria under hypoxia. Mitochondria-localized GPCPD1 could hamper VDAC1 homo-oligomerization, which triggered mitophagy through polyubiquitination of VDAC1 by PRKN. We further investigated GPCPD1-mediated hypoxia-induced mitophagy during TNBC progression.

## Results

### Screening and identification of GPCPD1 as a regulator of hypoxia-induced mitophagy

To explore the key modulators of mitophagy, we utilized the mitochondria-localized fluorescent protein mt-Keima to screen for mitophagy activity. Changes in green to red fluorescence are indicative of mitophagy (Figure S1A). In addition, dual staining with both mt-Keima and MitoTracker probes ensured the specific localization of mt-Keima to mitochondria, with representative confocal images displaying a perfect overlap of these two labeling methods (Figure S1B). We detected a notable elevation in the red to green fluorescence ratio induced by hypoxia (1% O<sub>2</sub>) and carbonyl cyanide 3-chlorophenylhydrazone (5 μM) in MDA-MB-468 (MDA468) cells expressing mt-Keima, indicating that

mitophagy had accumulated over time (Figure 1A and Figure S1C). TOMM20 staining indicated that mitochondrial quantification was drastically reduced under hypoxic conditions and CCCP treatment, which is inconsistent with previous findings (Figure 1A and Figure S1D). To screen the potential regulators of hypoxia-induced mitophagy, genes expressed differentially in hypoxia (1% O<sub>2</sub>, 48 h) and CCCP treatment (5 μM, 48 h) were evaluated by RNA-seq in two TNBC cell lines (MDA468 and MDA231) (Figure 1B). We then intersected the differentially expressed gene list from RNA-seq with the HIF1A target gene list from HIF1A chromatin immunoprecipitation (ChIP-seq) (Figure 1C, Table S1-3), as the response to hypoxia is largely due to the transcriptional activity of HIF1A [14]. There were 18 genes at the end of the intersection, and we validated their mRNA expression in both lines using quantitative polymerase chain reaction (qPCR). Out of the 18 candidate genes, we selected six genes (*ATF3*, *DNAJB9*, *GPCPD1*, *KDM7A*, *PNRC1*, and *TRIB3*) whose mRNA expression increased twice-fold following hypoxia and CCCP treatment (Figure 1D). Finally, we applied mt-Keima-based flow cytometry to quantify hypoxia or CCCP-triggered mitophagy after knocking down these six candidate genes individually in MDA468 cells expressing mt-Keima (Figure 1E-G). GPCPD1 was identified as one of the most significant regulators of mitophagy. As expected, mitophagy was significantly reduced after *TRIB3* and *ATF3* knock-down (Figure 1E-G). *ATF3* and *TRIB3* have been reported to be key players in mitophagy [15,16], which verified that our screening strategy was reliable.

GPCPD1 hydrolyzes glycerophosphocholine to choline and glycerol-3-phosphate and thus plays a key role in choline metabolism [17,18]. To evaluate its role in hypoxia-induced mitophagy, we treated MDA231 and MDA468 cells with hypoxia, CCCP, and cyclosporine (CsA) for specified time points. We detected a remarkably increased expression of *GPCPD1* mRNA and protein with both hypoxia and CCCP treatment, whereas *GPCPD1* decreased significantly with CsA treatment (Figure 1H and I, Figure S1E-G). Furthermore, we knocked down HIF1A in two cell lines, treated with and without hypoxia, and found that silencing of HIF1A significantly decreased the mRNA and protein levels of GPCPD1. Notably, hypoxia magnified the regulatory effect of HIF1A on *GPCPD1* expression (Figure 1J and K, Figure S1H). These findings suggest that *GPCPD1* is a key regulator of hypoxia-induced mitophagy.

### GPCPD1 was transcriptionally regulated by HIF1A with the assistance of H3K4me3 and H3K27ac

Next, we explored the regulatory mechanism of *HIF1A* in *GPCPD1* cells. Consistent with the results mentioned above, we found a positive relationship between *GPCPD1* and *HIF1A* mRNA expression in the patient data from the METABRIC database (Figure 2A). Further bioinformatics predictions from multiple databases indicated that HIF1A is a transcriptional factor of *GPCPD1* (Figure 2B, Table S4). To verify the transcriptional regulation of HIF1A on *GPCPD1*, we first selected the top three hypoxia response elements (HREs) residing in the *GPCPD1* promoter region according to the prediction

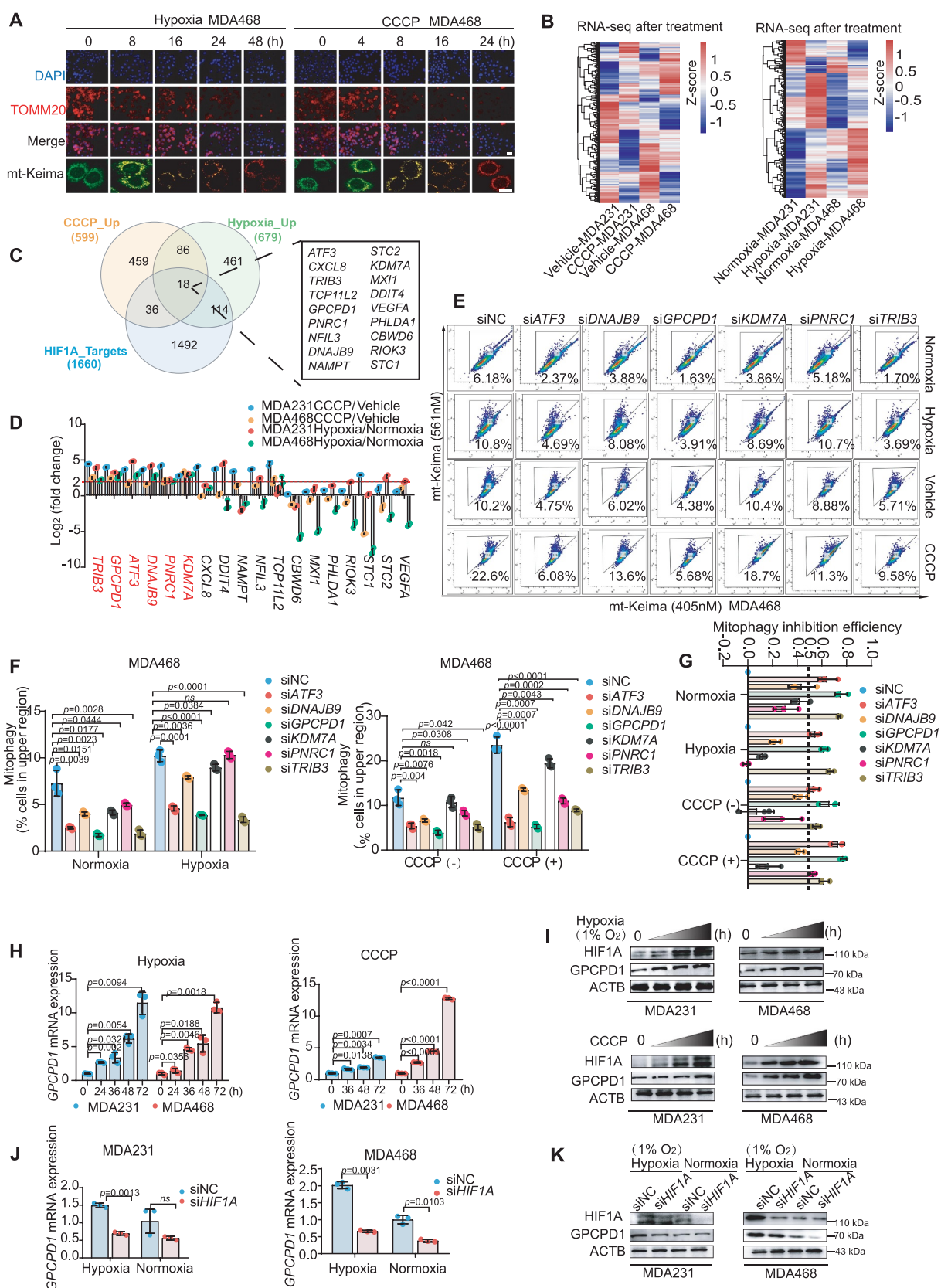


**Figure 1.** Screening and identification of *GPCPD1* as a regulator of hypoxia-induced mitophagy. (A) Representative immunofluorescence analysis of TOMM20 (top) and mt-Keima (bottom) in MDA-MB-468 (MDA468) cells. Scale bar for TOMM20 images: 50  $\mu$ m; Scale bar for mt-Keima images: 100  $\mu$ m. (B) Heatmaps of differentially expressed genes in MDA-MB-231 (MDA231) and MDA468 cells with RNA-Seq analysis. (Z-score with  $\log_2$  scale from -1 to +1). (C) Venn diagram of overlap among upregulated genes from (B) and list of HIF1A target genes. Candidate genes are listed on the right panel. (D) Quantitative real-time PCR analysis of mRNA expression for indicated genes in MDA231 and MDA468 cells. The red dotted line indicated the fold change of  $\log_2 = 2$ . (E-G) Flow cytometry analysis of mt-Keima in MDA468



scores in the JASPAR database, and luciferase reporter constructs were generated by inserting different lengths of the *GPCPD1* promoter sequence (Figure 2C). The luciferase assay showed that, under hypoxic conditions, the luciferase activity of all three HREs was significantly increased (Figure 2C). Next, we observed a significant enrichment of HIF1A binding to the predicted HRE sites compared to immunoglobulin G controls using ChIP-qPCR assays, suggesting that *GPCPD1* was a direct target of HIF1A (Figure 2D). Collectively, these data suggest that under hypoxic conditions, HIF1A transcriptionally upregulates *GPCPD1* expression.

In this study, we noticed an interesting phenomenon: *GPCPD1* mRNA upregulation by hypoxia could only last for three days and rapidly reduced after 72 h. Several studies have shown that histone methylation and acetylation markers increase in mammalian cells exposed to severe hypoxia [19–21]. We then screened several histone methylation and acetylation markers for their peaks in the *GPCPD1* promoter region by analyzing the public ChIP-seq database and observed significant enrichment of H3K4me3 and H3K27ac in the *GPCPD1* promoter region (Figure S2A and Figure 2E). Therefore, we treated MDA231 and MDA468 cells with trichostatin (a deacetylation inhibitor) or 5-azacytidine (5-aza, a methylation inhibitor), respectively, under hypoxic or normoxic conditions and observed an increased transcriptional activity of *GPCPD1* with both trichostatin and 5-aza treatment, especially under hypoxic conditions (Figure 2F and Figure S2B and S2C). We then applied the ChIP-qPCR assay to dynamically estimate the enrichment of H3K4me3 and H3K27ac at the HREs site within the *GPCPD1* promoter region. The results demonstrated that hypoxia could enrich H3K4me3 at the HREs site in the *GPCPD1* promoter region; enrichment peaked at 24 h and vanished by 72 h (Figure 2G). We observed a similar result in the corresponding experiment for H3K27ac, with enrichment peaking at 48 h and vanishing by 96 h (Figure 2H). In summary, these findings suggest that H3K4me3 and H3K27ac facilitate dynamic hypoxia-mediated transcription of *GPCPD1*.

### ***GPCPD1*-regulated tumor progression and chemotherapy resistance in TNBC cells under hypoxic conditions**

It has been widely recognized that hypoxia results in tumor progression and chemotherapy resistance, leading to a poorer prognosis [22]. To determine the effect of *GPCPD1* on the progressive features and chemotherapy resistance of TNBC cells under hypoxic conditions, we established stably transfected cell lines (MDA231 and MDA468) with *GPCPD1* overexpression or knockdown. We found that the proliferation rate of both cell types increased more under hypoxia than under normoxia, which was in accordance with previous evidence [23–25]. While silencing of *GPCPD1* significantly

suppressed proliferation in both cell types compared to their corresponding controls. Overexpression of *GPCPD1* significantly increased the proliferation rate of both cells compared to that of the relative controls (Figure 2I). Additionally, the EdU assay showed that overexpression of *GPCPD1* enhanced hypoxia-induced proliferation. In contrast, the knockdown of *GPCPD1* alleviated this effect in TNBC cells (Figure S2D and S2E). We then assessed the effect of *GPCPD1* on metastasis and found that *GPCPD1* silencing reduced hypoxia-promoted migration (Figure 2J and K), which further demonstrated that *GPCPD1* plays an important role in facilitating TNBC cell proliferation, especially under hypoxic conditions.

Doxorubicin (DOX) is a major first-line chemotherapeutic drug used for treating TNBC [26]. We observed a significant increase in *GPCPD1* protein expression in DOX-resistant MDA231 cells (Figure S2F). Therefore, we investigated whether *GPCPD1* affects chemotherapeutic resistance to DOX in TNBC cells. We found that the knockdown of *GPCPD1* decreased the cellular viability to DOX treatment, while overexpression of *GPCPD1* significantly increased the cellular viability to DOX treatment in both MDA231 and MDA468 cells (Figure S2G). *GPCPD1* overexpression had a similar effect on cell migration after DOX treatment. We found that ectopic expression of *GPCPD1* helped maintain the metastatic ability of TNBC cells under DOX treatment, whereas silencing of *GPCPD1* combined with DOX treatment significantly reduced migration in both cell lines (Figure S2H and S2I). Collectively, our results imply that *GPCPD1* may be a useful target for overcoming chemotherapeutic resistance in patients with TNBC.

### ***GPCPD1* played an important role in hypoxia-induced mitophagy in TNBC cells**

Considering that *GPCPD1* was first identified as the key regulator of choline metabolism and that the effect of *GPCPD1* in mitophagy has not been reported or explored before, we applied high-throughput RNA-seq in both MDA468 and MDA231 cells transfected with siRNA against *GPCPD1* or non-targeted siNC (Figure 3A). To examine the involvement of *GPCPD1* in mitophagy, we conducted a Gene Ontology analysis and, as expected, we consistently found that *GPCPD1* was associated with multiple mitochondria-related terms including “mitochondrial protein complex”, “mitochondrial gene expression”, and “mitochondrial inner membrane” (Figure 3B). Furthermore, GSEA analysis showed that *GPCPD1* knockdown greatly suppressed choline metabolism, autophagy, and mitophagy-related pathways, which confirmed our previous results that *GPCPD1* was superior to mitophagy in full play (Figure 3C, Figure S3A, Table S5). To verify that *GPCPD1* could influence mitochondrial metabolism and mitophagy in TNBC cells, we performed a Seahorse

cells with indicated genes knockdown. Mitochondria in the cytosol were represented by mt-Keima with an excitation of 405 nm, while mitochondria in lysosomes were represented by mt-Keima with an excitation of 561 nm. Mitophagy is reflected by the percentage of cells in the upper region. Numbers in the cytometry charts indicate the percentages of corresponding subpopulations. Quantification (E) and statistical diagrams (F) of cells in the upper gated region. (G) The mitophagy inhibition efficiency was defined as significant when the value of mitophagy inhibition efficiency was more than 0.5. (H) Quantitative real-time PCR (qPCR) analysis of *GPCPD1* mRNA levels in MDA231 and MDA468 cells. (I) Western blot analysis of *GPCPD1* and HIF1A in MDA231 and MDA468 cells. (J) The qPCR analysis of *GPCPD1* mRNA levels in MDA231 and MDA468 cells with the *HIF1A* knockdown. (K) Western blot analysis of *GPCPD1* and HIF1A in MDA231 and MDA468 cells with *HIF1A* knockdown. Cells of all the experiments mentioned above were treated with hypoxia (1% O<sub>2</sub>) or CCCP (5 μM) as indicated. (D, F, H, J) Two-tailed unpaired t-test.



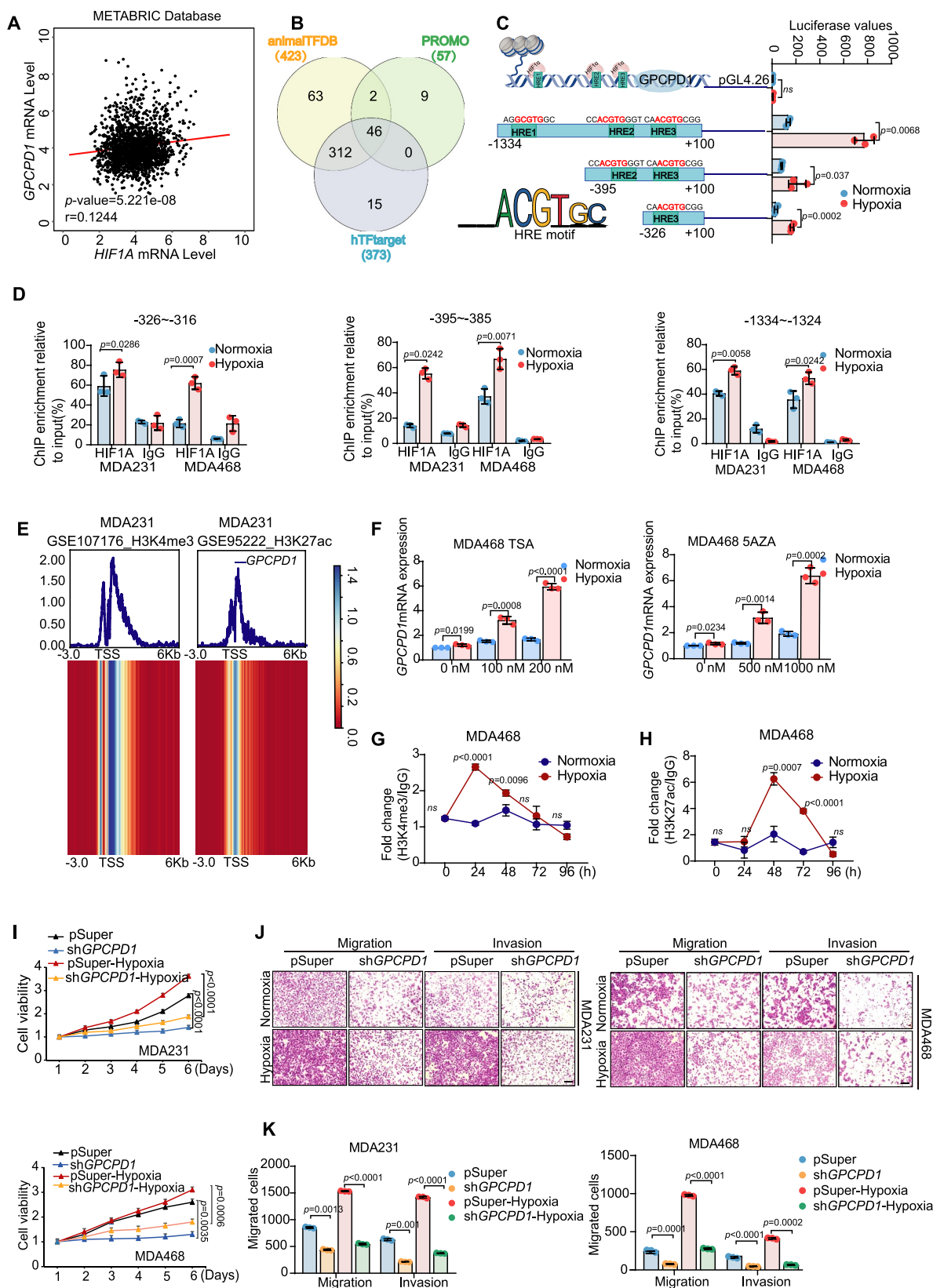


**Figure 2.** *GPCPD1* was transcriptionally regulated by HIF1A with the assistance of H3K4me3 and H3K27ac. (A) The scatter plot of the correlation between *GPCPD1* and *HIF1A* mRNA from the METABRIC database.  $p = 5.221 \times 10^{-8}$ ,  $r = 0.1244$ . (B) HIF1A was identified as a transcription factor of *GPCPD1* after intersection analysis. (C) Luciferase activity of wild-type or truncated *GPCPD1* promoter in 293 T cells treated with hypoxia. (D) ChIP assay of enrichment of HIF1A on the *GPCPD1* promoter. (E) ChIP-seq heatmap of the strong signal of H3K4me3 and H3K27ac on the *GPCPD1* promoter region. (F) The qPCR analysis of *GPCPD1* mRNA levels in MDA231 and MDA468 with indicated concentrations of TSA and 5-aza under hypoxia or not. (G and H) ChIP assay of enrichment of H3K27ac (G) and H3K4me3 (H) on the *GPCPD1* promoter in MDA468 cells in a time gradient. (I) Cell variability in MDA231 and MDA468 cells with *GPCPD1* knockdown. (J and K) Transwell migration and invasion assays in MDA231 and MDA468 cells with *GPCPD1* knockdown. Representative areas of invaded cells stained with crystal violet are shown and invaded cells of three random fields were quantitatively analyzed. Scale bar: 20  $\mu\text{m}$ . (C, D, F-K) Cells in these experiments were treated with hypoxia (1%  $\text{O}_2$ ) or not as indicated. (C, D, F-I, K) Two-tailed unpaired t-test.

experiment to measure the oxidative phosphorylation rate. As shown in Figure 3D and E, the knockdown of *GPCPD1* effectively decreased the O<sub>2</sub> consumption rate (OCR) of TNBC cells, while overexpression of *GPCPD1* effectively increased the OCR of TNBC cells, which implied that *GPCPD1* could induce oxidative metabolism in TNBC cells. We also found that *GPCPD1* knockdown retarded reactive oxygen species generation, whereas hypoxia enhanced this retarded effect (Figure 3F and Figure S3B). Furthermore, we found that overexpression of *GPCPD1* led to a significant rescue of mitochondrial membrane potential ( $\Delta\psi_m$ ) and ATP level, as well as enhanced the extent of mPTP (mitochondrial permeability transition pore) shutting under hypoxic conditions (Figure 3G and Figure S4C and S4D). In addition, we also found that CQ treatment decreased  $\Delta\psi_m$ , ATP level, and enhanced the extent of mPTP opening in TNBC cells overexpressing *GPCPD1* under hypoxic conditions (Figure S3E-G). And then immunofluorescence showed that TOMM20, a mitochondrial marker, decreased with *GPCPD1* overexpression, especially under hypoxic conditions. In contrast, TOMM20 increased after the silencing of *GPCPD1* (Figure S3H and S3I). Considering that dynamic change of the mitochondrial membrane is related to continuous fission and fusion [27], we then explored whether *GPCPD1* could influence the fission and fusion of mitochondria. In concert with cell fate, mitochondrial fusion is thought to protect cells against death and is closely related to mitophagy [28]. Immunofluorescence showed that MFN1, a mitochondrial fusion marker, was increased with *GPCPD1* overexpression and was decreased with *GPCPD1* silence in TNBC cells treated with hypoxia (Figure S3J and S3K). We also treated TNBC cells with CQ in hypoxic conditions, a fusion inhibitor between autophagosomes and lysosomes, and a western blot assay indicated that MFN1 and MFN2 were significantly increased after being treated with CQ. We then found that *GPCPD1* overexpression could reduce mitochondrial fusion with increased expression of MFN1 and MFN2 and decreased mitochondrial fission with downregulation of FIS1 in hypoxic conditions. In consistent with these results, *GPCPD1* silence hampered mitochondrial fusion with the downregulation of MFN1 and MFN2 and enhanced mitochondrial fission with the upregulation of FIS1 (Figure S3L). All these results indicated that *GPCPD1* played an important role in maintaining mitochondrial membrane integrity and ATP production during hypoxic stress. Furthermore, upregulated *GPCPD1* increased MT-ND2 (complex I), MT-CYB/CYTB (complex III), and MT-CO2/COX2 (complex IV) under hypoxic conditions, but CQ decreased the protein levels of mitochondrial respiratory complexes following hypoxia treatment (Figure S4A), consistent with the immunofluorescence results for MT-CO2/COX2 (Figure S4B and C). All these results indicated that *GPCPD1* could regulate mitochondria quantity and quality under hypoxic stress, thus contributing to the mitophagy process.

Furthermore, we utilized fluorescent mt-Keima in the mitochondria to detect mitophagy activity after overexpression or knockdown of *GPCPD1* (Figure 3H and Figure S4D). Microscopic analysis revealed that the ratio of red to green fluorescence was markedly increased in *GPCPD1*-

overexpressing cells under hypoxia. In contrast, the red to green fluorescence ratio decreased in *GPCPD1*-knockdown cells under hypoxic conditions. Meanwhile, Electron microscopy was used to assess autophagosomes in MDA231 cells 48 h after hypoxia. In control cells, autophagosomes were enclosed by typical double membranes (indicated by red arrows), and entire organelles (possibly mitochondria) were occasionally present. In contrast, *GPCPD1*-knockdown cells showed few autophagosomes or autolysosomes (Figure 3I and Figure S4E), suggesting that mitophagy might be suppressed by silencing *GPCPD1* expression. Mitophagy flux is considered of great importance as both protective and detrimental functions in cancer progression.

We further evaluated mitophagy flux and the results showed that overexpression of *GPCPD1* promoted while knockdown of *GPCPD1* suppressed the increased LC3B protein levels induced by hypoxia or/and CQ treatment (Figure 3J and Figure S4F). A greater number of LC3B puncta were visible in *GPCPD1*-overexpressing TNBC cells than in the controls after hypoxia or/and CQ treatment, as shown by immunofluorescent LC3B staining (Figure 3K and 3L), indicating the critical role of *GPCPD1* in mitophagy flux.

Next, we examined whether *GPCPD1*-mediated mitophagy could regulate TNBC cell proliferation and metastasis. We overexpressed *GPCPD1* in TNBC cells and then treated cells with CQ to inhibit mitophagy. And then we performed MTT, Edu, and transwell assays and found that CQ treatment inhibited *GPCPD1*-promoted proliferation and metastasis in TNBC cells (Figure S5A-E). In addition, we also overexpressed or silenced *GPCPD1* in TNBC cells and then treated cells with CCCP to activate or CsA to inhibit mitophagy. Using the Edu assay, we observed that the inhibition of cell growth via knockdown of *GPCPD1* was reversed by CCCP treatment in both MDA231 and MDA468 cells, while the promotive effect on cell proliferation by *GPCPD1* overexpression diminished with CsA treatment (Figure S5F and S5G). In addition, we observed similar results in migration and invasion assays (Figure S5H and S5I), implying that mitophagy plays an essential role in TNBC growth and metastasis. And protein level of TOMM20 and LC3B indicated that *GPCPD1* regulates TNBC growth and metastasis via mitophagy (Figure S5J).

### Depalmitoylation of *GPCPD1* appeared to have an affinity to mitochondria

We then investigated how *GPCPD1* exerted its robust action on mitophagy initiation. We detected increased expression of FUNDC1, BNIP3L, BNIP3, and PINK1-PRKN under hypoxia; however, *GPCPD1* overexpression and knockdown did not alter the protein expression levels of FUNDC1, BNIP3L, BNIP3, or PINK1-PRKN under hypoxic or normoxic conditions (Figure S4G), indicating that *GPCPD1* may not regulate the canonical pathways that participate in hypoxia-induced mitophagy. The Gene Ontology analysis from RNA-seq data demonstrated that *GPCPD1* was significantly associated with the mitochondria-related cellular compartment terms, making us wonder whether *GPCPD1* exerts its function in mitophagy via locating mitochondria. Using a subcellular fractionation

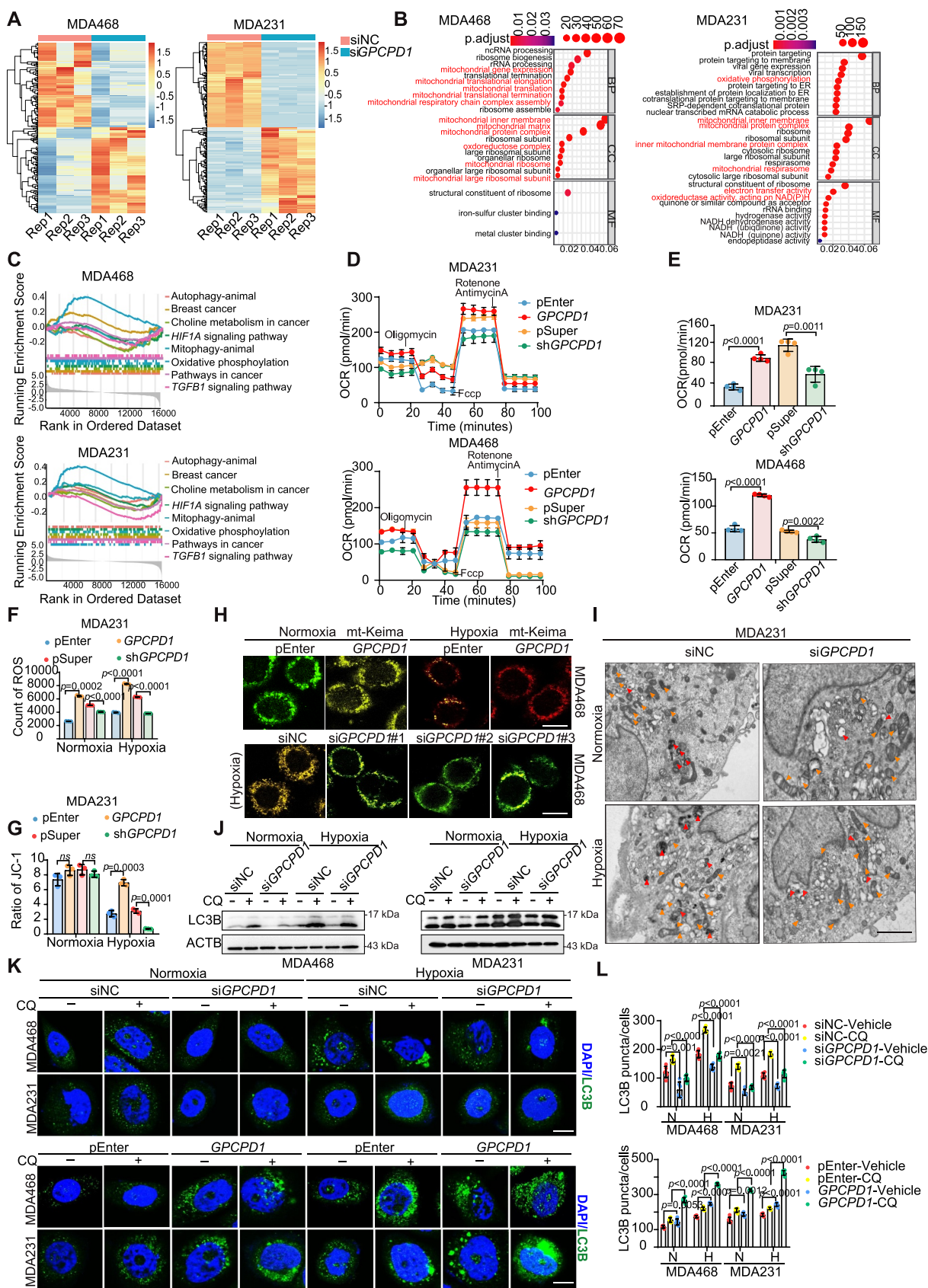


**Figure 3.** *GPCPD1* was required for hypoxia-induced mitophagy. (A) Heatmaps of the differentially expressed genes in MDA231 and MDA468 cells regulated by *GPCPD1* with RNA-Seq analysis. (B) GO analysis (mitochondrial-associated clusters are marked by red) and (C) GSEA analysis for (A). (D) Oxygen consumption rate (OCR) alterations in MDA231 and MDA468 cells with *GPCPD1* overexpression or knockdown. (E) Quantification of mitochondrial respiration capacity in (D). (F and G) ROS (F) and JC-1 (G) in MDA231 cells with *GPCPD1* overexpression or knockdown. (H) Immunofluorescence analysis of mt-Keima in MDA468 cells. Scale bar: 100  $\mu$ m. (I) Electron microscopy images of MDA231 cells with *GPCPD1* knockdown. Scale bar: 5  $\mu$ m. Damaged mitochondria, Orange arrows; autophagosomes, red arrows. (J) Western blot analysis of LC3B in MDA231 and MDA468 cells with indicated treatments. (K and L) Immunofluorescence analysis (K) and quantification (L) of LC3B staining in MDA231 and MDA468 cells. Scale bar: 100  $\mu$ m. (F-H and J, K) Cells in these experiments were treated with hypoxia (1% O<sub>2</sub>) or not as indicated. (E-G, L) Two-tailed unpaired t-test.



assay, we found a significant enrichment of GPCPD1 within the cytoplasm, especially in mitochondria, under hypoxic conditions compared to normoxic conditions, suggesting that there might be dynamic trafficking of GPCPD1 from the cytosol to mitochondria under hypoxic conditions (Figure 4A and Figure S6A). Immunofluorescence also indicated that hypoxic conditions could influence the localization of GPCPD1 to the mitochondria with an increase in yellow speckles (Figure 4B). According to previous studies, the accommodation of subcellular localization between the cytomembrane and the OMM can be regulated by the palmitoylation/depalmitoylation cycle [29]. With the *in silico* prediction of protein-protein interactions, we detected an interaction between GPCPD1 and LYPLA1 (lysophospholipase 1), as well as LYPLA2 (Figure S6B), which are key regulators of the depalmitoylation process, by adjusting the hydrophobicity and cellular localization of the target proteins [30,31]. Co-immunoprecipitation (co-IP) assays in MDA468 cells indicated that only endogenous LYPLA1 could interact with endogenous GPCPD1 (Figure 4C). It has also been reported that LYPLA1 but not LYPLA2 could exist in mitochondria after depalmitoylation activation [32]. Next, we performed a co-IP assay with ectopic Flag-GPCPD1 and MYC-LYPLA1 and confirmed the interaction between GPCPD1 and LYPLA1 in 293 T cells (Figure 4(D and E)). We then performed a co-IP assay with antibody capture and detection of endogenous GPCPD1 or LYPLA1 and confirmed the affinity between endogenous LYPLA1 and endogenous GPCPD1 in TNBC cells (Figure 4F). In addition, a public database that can predict palmitoylation modifications of proteins revealed that GPCPD1 has three palmitoylation sites (Figure S6C), and with an acylbiotin exchange assay, we confirmed that the cysteine residues of GPCPD1 could be palmitoylated in TNBC cells (Figure 4G). We then impeded the depalmitoylation process by palmostatin B (PalmB, a potent inhibitor of depalmitoylation) and siLYPLA1 in MDA468 cells under hypoxia and found that depalmitoylation inhibition could result in the separation of GPCPD1 from mitochondria, presenting as the disappearance of the yellow speckles (Figure 4H and 4I). The mitochondrial isolation assay suggested that the GPCPD1 protein localized to the mitochondria significantly decreased after treatment with PalmB, especially under hypoxic conditions (Figure 4J and Figure S6D). Collectively, our results demonstrate that depalmitoylated GPCPD1 has a strong affinity for mitochondria.

### VDAC1 was identified as the counterpart of GPCPD1 during mitophagy

We used LC-MS to identify the counterparts of GPCPD1 in hypoxia-induced mitophagy. Quantification of GPCPD1-interacting proteins using LC-MS revealed that 27 proteins might specifically interact with GPCPD1 under hypoxic conditions. We then intersected the above protein list from LC-MS with the mitophagy-related protein list from the interactome database and found that VDAC1 (voltage dependent anion channel 1) was the only one among the intersections (Figure 5A). VDAC1, located on the OMM, modulates both energy and metabolic exchanges within mitochondria and

plays an essential role in mitochondria-mediated autophagy [33]. We then predicted the interaction between GPCPD1 and VDAC1 in a 3D structure (Figure 5B), which indicated that GPCPD1 could bind to the  $\beta$ -strand of VDAC1, which might interfere with the oligomerization of VDAC1. In addition, we found that VDAC1 largely colocalized with GPCPD1, indicating binding between the two proteins (Figure 5C). To confirm this under hypoxic conditions, we performed co-IP assays using GPCPD1- and VDAC1-expressing 293 T cells. As shown in Figure 5D, ectopic GPCPD1 effectively co-immunoprecipitated with ectopic VDAC1. We performed co-IP assays in MDA468 cells after ectopic expression of MYC-VDAC1 or Flag-GPCPD1. Our data showed that ectopic VDAC1 was immunoprecipitated with endogenous GPCPD1 and vice versa (Figure 5E). Moreover, we proved that endogenous GPCPD1 could significantly bind to endogenous VDAC1 in MDA468 cells (Figure 5F). Considering the affinity of depalmitoylated GPCPD1 for mitochondria, we investigated whether the palmitoylation/depalmitoylation process could influence the binding capacity between GPCPD1 and VDAC1. In the co-IP assay of MDA468 cells expressing ectopic VDAC1, treatment with PalmB, ML348 (a specific LYPLA1 inhibitor), or siLYPLA1 significantly diminished the interactions between endogenous GPCPD1 and ectopic VDAC1 (Figure 5G). Immunofluorescence also showed that depalmitoylation inhibition could influence the colocalization of GPCPD1 and VDAC1 with decreased yellow speckles (Figure 5H and Figure S6E). These results demonstrate that GPCPD1, which is located on the OMM, interacts with VDAC1 during mitophagy and that the interaction between GPCPD1 and VDAC1 could be regulated by depalmitoylation.

GPCPD1 comprises an N-terminal CBM20 domain (also known as the starch-binding domain) and a GDPD\_GDE5 domain (the glycerophosphodiester phosphodiesterase domain). To map the region within GPCPD1 that mediates its interaction with VDAC1, two mutants with only a CBM20 or GDPD\_GDE5 domain were constructed (Figure 5I). We conducted a co-IP assay in 293 T cells and found significant binding of the Flag-CBM20 construct to the full-length VDAC1, but failed to detect any binding capacity of the GDPD\_GDE5 construct to VDAC1, demonstrating that it is the CBM20 domain of GPCPD1 that binds to VDAC1 (Figure 5J). VDAC1 belongs to the Porin3 superfamily of  $\beta$ -barrel transmembrane proteins [34]. According to the mass spectrometry results, the predicted binding sequence of VDAC1 to GPCPD1 is "LTLSALLDGK," which is located in the  $\beta$ -18 strand of VDAC1 (Figure 5A). It is predicted that the  $\beta$ -18 strand of VDAC1 is associated with oligomerization [35,36]. The conserved domain architecture retrieval tool predicted that leucine residues in the  $\beta$ -18 strand of VDAC1 are conserved across different species, indicating that leucine residues are essential for the oligomerization of VDAC1 (Figure 5K). We then constructed VDAC1 mutants by substituting two conserved leucines (L257 and L259) with alanine (L257A L259A) and performed co-IP assays in 293 T cells ectopically expressing wild-type (WT) VDAC1 or VDAC1 with L257A L259A mutations. When comparing wild-type VDAC1 and VDAC1 with L257A L259A mutations, we

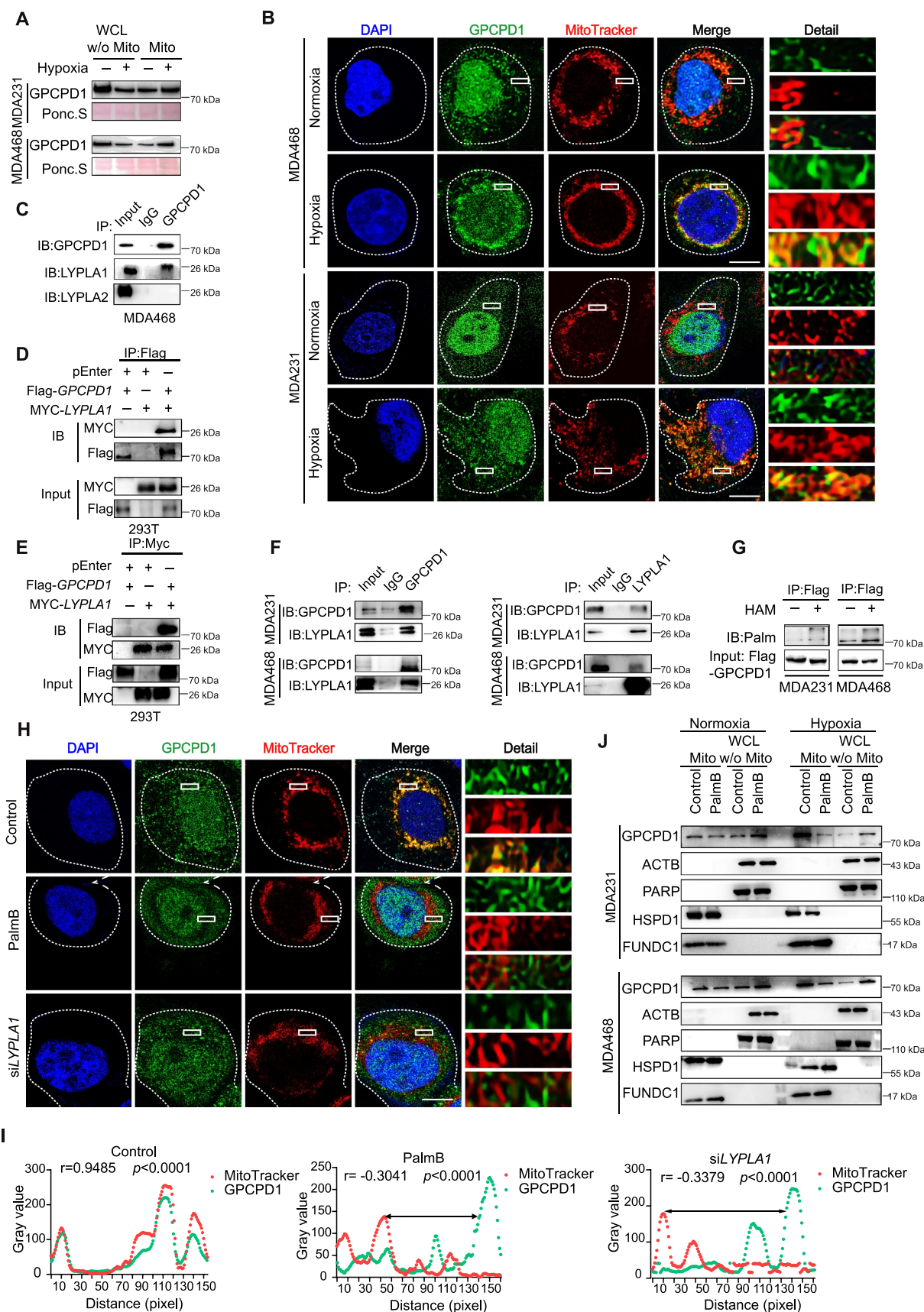


**Figure 4.** Depalmitoylation of GPCPD1 appeared to have a close affinity to mitochondria. (A) GPCPD1 protein levels in the mitochondrion fraction (Mito) and whole-cell lysates without mitochondrion fraction (WCL w/o Mito). (B) Immunofluorescence analysis of GPCPD1 and MitoTracker in MDA231 and MDA468 cells. Scale bar: 100  $\mu$ m. (C) The co-IP assay proved the interactions between GPCPD1 with LYPLA1 not with LYPLA2 in MDA468 cells. IB, immunoblot. (D and E) The co-IP assay was performed to detect the exogenous GPCPD1-LYPLA1 interaction in 293 T cells with ectopic *GPCPD1* or/and *LYPLA1* expression. (F) A co-IP assay was performed to detect the endogenous GPCPD1-LYPLA1 interaction in MDA231 and MDA468 cells. (G) The ABE assay of S-acylated GPCPD1 in MDA231 and MDA468 cells. The

found that VDAC1 with L257A L259A mutations had a reduced binding capacity for both the full-length GPCPD1 and CBM20 domains (Figure 5L). Altogether, these results demonstrate that the CBM20 domain of GPCPD1 interacts with VDAC1, and 257259leucine residues of the VDAC1 protein play an important role in the interaction of VDAC1 and GPCPD1.

We also examined whether *GPCPD1* enhances TNBC metastasis by interacting with *VDAC1*. We silenced *GPCPD1* in MDA468 cells and overexpressed *VDAC1* in them. Using a colony formation assay, we observed an inhibitory effect on colony formation after *GPCPD1* knockdown, which was reversed by *VDAC1* overexpression (Figure S7A), whereas the promotive effect on cell migration with *GPCPD1* overexpression was attenuated by *VDAC1* silencing in TNBC cells (Figure S7B). This suggests that *GPCPD1* regulates tumor proliferation and metastasis by interacting with *VDAC1*.

### ***GPCPD1 promoted mitophagy by interfering with the oligomerization of VDAC1***

The aforementioned prediction from the conserved domain architecture retrieval tool indicates that the binding sequence of VDAC1 to GPCPD1 might be associated with the monomer-oligomer homeostasis of VDAC1. Thus, we knocked down *GPCPD1* with incremental concentrations of siRNA in TNBC cells and found that it significantly increased the formation of VDAC1 trimers and other oligomers (Figure 6(A and B) and Figure S6F). In addition, studies have reported that PRKN-mediated polyubiquitination of VDAC1 mediated by PRKN could induce mitophagy [37]. Therefore, we considered that the monomer-oligomer homeostasis of VDAC1 could affect PRKN-mediated ubiquitination and, thereby, mitophagy. We first showed that VBIT-4, a VDAC1 oligomerization inhibitor, could induce full activation and monomerization of VDAC1 in TNBC cells over a time gradient (Figure 6(C and D) and Figure S6G). Next, we performed co-IP assays in MDA468 cells with ectopic expression of HA-*Ub*, MYC-*VDAC1*, and HA-*PRKN*, with or without treatment with VBIT-4. Our data showed that more ubiquitination modification of VDAC1 by PRKN was detected in the presence of VBIT-4, suggesting that VDAC1 monomers recruited more PRKN-mediated polyubiquitination than oligomers (Figure 6E). Moreover, knockdown or overexpression of *GPCPD1* in TNBC cells influenced the colocalization of VDAC1 and PRKN with a reduction or increase in yellow speckles, and VBIT-4 treatment promoted the colocalization of VDAC1 with PRKN, suggesting that monomers of VDAC1 facilitated the interaction with PRKN (Figure 6(F and G) and Figure S7C). In conclusion, we demonstrated for the first time that *GPCPD1* interferes with the oligomerization of VDAC1, thus generating more anchor sites to recruit PRKN-mediated

polyubiquitination, which promotes mitophagy in TNBC cells.

In addition, our previous results showed that upregulated or downregulated *GPCPD1* did not influence the protein level of PRKN in either normoxic or hypoxic conditions, but the whole level of PRKN protein increased with hypoxia treatment. Nevertheless, with the subcellular fractionation assay, we found a significant decrease in PRKN protein in the mitochondrial fraction with *GPCPD1* knockdown compared to the control group under hypoxic conditions, suggesting that *GPCPD1* contributed to the dynamic trafficking of PRKN from the cytosol to mitochondria. LC3B expression also decreased with *GPCPD1* silencing in the mitochondrial fraction (Figure S7D). Furthermore, to explore the significance of *GPCPD1*-PRKN activation by hypoxia in TNBC cells, we transfected *PRKN* siRNA in mt-Keima-MDA468 cells overexpressing *GPCPD1* and found that si*PRKN* hampered mitophagy in *GPCPD1* overexpressing MDA468 cells under hypoxic conditions (Figure S7E and 7F). Subsequently, we also examined the effect of si*PRKN* on cell proliferation and metastasis in *GPCPD1* overexpressing cells and the results showed that downregulation of PRKN could abolish the promotive effect of *GPCPD1* on cell proliferation and metastasis of TNBC cells under hypoxic conditions (Figure S7G-M). In summary, our results suggest that *GPCPD1* contributes to mitophagy in TNBC cells by regulating the VDAC1-PRKN axis under hypoxic conditions.

### ***GPCPD1 could serve as an independent prognostic marker in breast cancer***

The function of *GPCPD1* was investigated *in vivo* by implanting *GPCPD1*-overexpressing and controlling MDA231 cells into the flank of BALB/c mice. These data indicated that *GPCPD1* overexpression significantly promoted tumor growth and resistance to DOX in MDA231 cells. In addition, we implanted *GPCPD1*-knockdown and control MDA231-Luc cells in the same manner. *GPCPD1* silencing enhanced the susceptibility of MDA231 cells to DOX (Figure 7A-C). Immunohistochemistry staining of xenograft tumors showed that silencing of *GPCPD1* significantly reduced the expression of the proliferation biomarker MKI67 (Figure S8A and S8B). To explore and verify the relationship between *GPCPD1* and HIF1A at the protein level, we observed accumulated *GPCPD1* expression in areas with abundant HIF1A expression, particularly in hypoxic central areas of xenografts. Conversely, we observed a deficiency of *GPCPD1* and HIF1A expression at tumor margins away from the hypoxic central regions (Figure 7D, Figure S8C). We also investigated the function of *GPCPD1* in lung metastases by the intravenous injection of MDA231 cells. Consistent with the *in vitro* results, *GPCPD1* knockdown reduced the degree of lung colonization by cells (Figure 7(E and F)). Furthermore,

absence of hydroxylamine (HAM) during the reaction was used as a reaction specificity control. (H and I) Immunofluorescence analysis of *GPCPD1* and MitoTracker in MDA468 cells with DMSO (control), 25  $\mu$ M palmB, or si*YPLA1* treatment respectively (under hypoxic conditions). Scale bar: 100  $\mu$ m. The merged images were analyzed by ImageJ to calculate the intensity variability (bottom). Two-tailed unpaired t-test. (J) *GPCPD1* protein levels of the mitochondrion and WCL w/o Mito after being treated with 25  $\mu$ M palmB or si*YPLA1*. ACTB and PARP represented cytoplasmic proteins excluding mitochondrion. FUNDC1 and HSPD1/HSP60 represented mitochondrial proteins. (A, B, J) Cells were treated in hypoxic conditions (1% O<sub>2</sub>) or not.



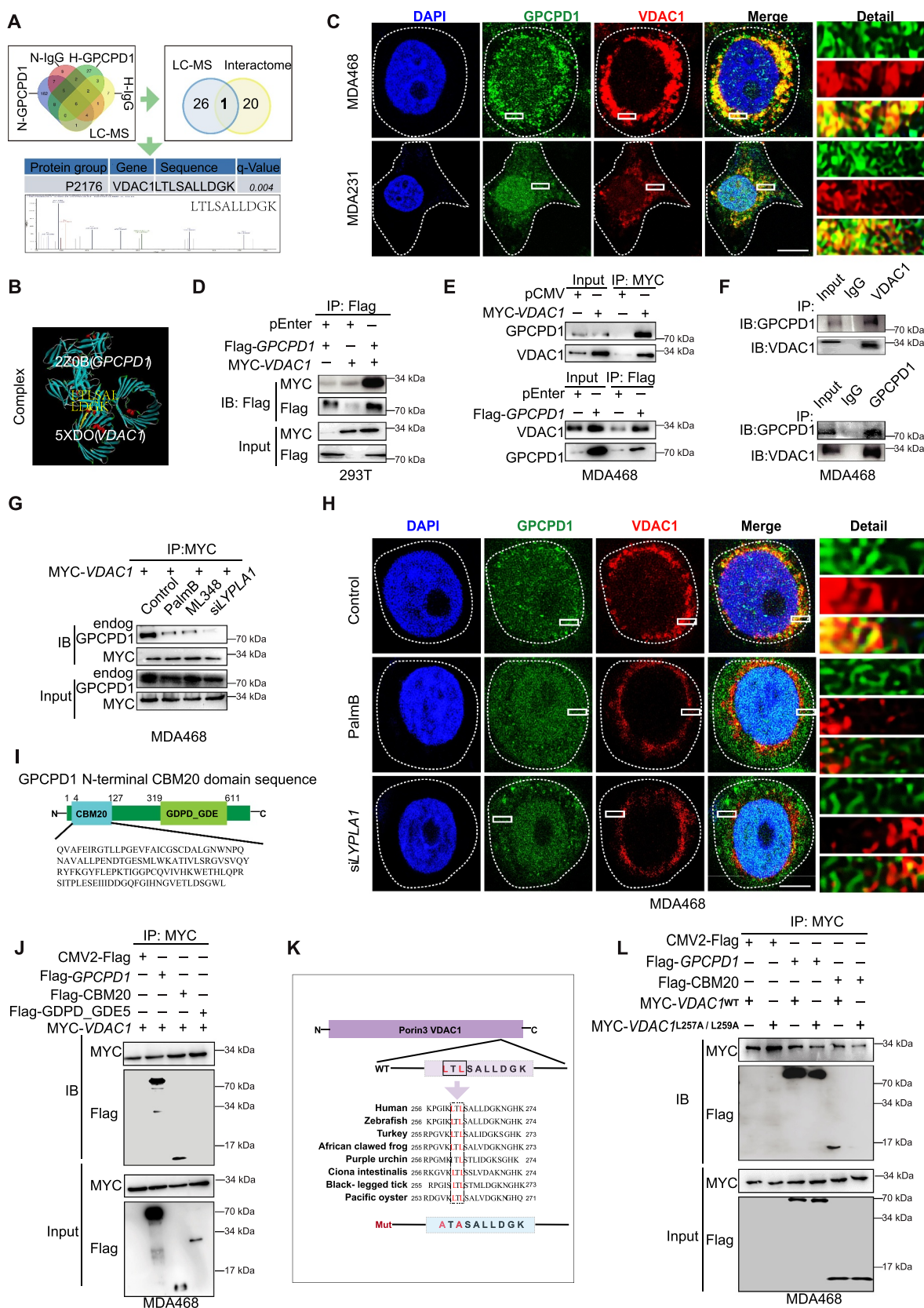


**Figure 5.** VDAC1 was identified as the counterpart of GPCPD1 during mitophagy. (A) The number of GPCPD1-interacting candidate proteins identified by co-IP LC-MS analyses in MDA468 cells. The data cluster mentioned above intersected with the data cluster from Reactome-mitophagy. VDAC1 was the only candidate protein. (B) 3D interaction model between GPCPD1 and VDAC1 predicted by ZDOCK Server. (C) Immunofluorescence analysis of GPCPD1 and VDAC1 in MDA231 and MDA468 cells (under hypoxic conditions). Scale bar: 100  $\mu$ m. (D) The co-IP assay was subjected to detect the exogenous GPCPD1-VDAC1 interaction in 293 T cells with ectopically expressed *GPCPD1* and *VDAC1*. (E) The co-IP assay was subjected to detect the GPCPD1-VDAC1 interaction in MDA468 cells with *VDAC1* overexpression (top) or *GPCPD1* overexpression (bottom) ectopically. (F) Co-IP assays proved the endogenous GPCPD1-VDAC1 interaction in MDA468 cells. (G) The co-IP assay was subjected to detect the altered GPCPD1-VDAC1 interactions in MDA468 cells, which were treated with DMSO (control), 25  $\mu$ M palmB, and 2  $\mu$ M *LYPLA1* inhibitor

overexpression of *GPCPD1* promoted DOX resistance in MDA231 cells, with increased lung metastatic nodes and shortened lifespans of nude mice. In contrast, nude mice inoculated with MDA231 cells with *GPCPD1* silenced survived significantly longer than controls (Figure 7G). Therefore, *GPCPD1* appears to play an oncogenic role in TNBC.

To further examine the clinical relevance of *GPCPD1*, we first detected the mRNA expression of *GPCPD1* in clinical breast specimens from Qilu Hospital of Shandong University and found that *GPCPD1* mRNA levels were significantly higher in tumor tissues ( $n = 72$ ) than in normal tissues ( $n = 72$ ) ( $p < 0.0001$ ) (Figure S8D). Furthermore, a high mRNA level of *GPCPD1* predicted a poor prognosis for overall survival in the Qilu cohort (Figure 7H). Next, we examined *GPCPD1* and HIF1A protein expression by immunohistochemistry on tissue microarrays and observed a high level of *GPCPD1* expression in samples with accumulated HIF1A proteins, indicating a positive correlation between *GPCPD1* and HIF1A expression ( $p = 0.0016$ , Figure S7I, and Figure S8E). These results are inconsistent with the finding that HIF1A transcriptionally regulates *GPCPD1* expression in TNBC. Additionally, the Kaplan-Meier survival plot demonstrated that higher *GPCPD1* expression was significantly associated with worse clinical outcomes ( $p = 0.012$ , Figure 7J). Lastly, we investigated the METABRIC database and found that increased *GPCPD1* and HIF1A levels were linked to both reduced overall survival and disease-free survival (Figure 7K). Multivariate Cox analysis and forest plots indicated that *GPCPD1* could serve as an independent prognostic marker in patients with TNBC (*GPCPD1* high vs. low, HR = 1.2 (1.01–1.3),  $p = 0.033$ , Figure S8F). Thus, these findings confirmed that *GPCPD1* exerts a promotive effect on the progression and metastasis of TNBC, which could act as a potential prognostic indicator in the future.

## Discussion

Overwhelming evidence has demonstrated that mitophagy is closely involved in the maintenance of mitochondrial integrity and functionality in cancer progression [5,38] and can be triggered by various stresses, including inflammation, nutrient deficiencies, and hypoxia [39,40]. Although multiple classical mitophagy regulators have been identified, the regulatory mechanism of mitophagy under hypoxic conditions remains largely unknown. Hypoxia is common in tumors, influences cell metabolic functions, and promotes metastasis [22]. In our study, we analyzed hypoxia-induced and CCCP-activated RNA-seq data, as well as HIF1A-targeted ChIP-seq data, and clarified that *GPCPD1* is required for hypoxia-induced mitophagy in TNBC by hampering VDAC1 oligomerization, which activates its polyubiquitination by PRKN. Thus,

*GPCPD1* functions as a regulator of mitophagy and thereby determines cancer development under hypoxia.

Hypoxia-induced alterations in the tumor microenvironment stimulate adaptive modifications in cells. Many of these adaptations are mediated by HIFs and HIF-1-associated pathways [41]. Moreover, HIF1A overexpression in several solid cancers is strongly associated with a poor prognosis [14]. Our data revealed that hypoxia increased HIF1A binding to the *GPCPD1* promoter region, and HIF1A could regulate *GPCPD1* expression at the transcriptional level. Interestingly, we also found that the mRNA expression of *GPCPD1* was downregulated after treatment with 1% O<sub>2</sub> for more than 72 h, which drew our attention to epigenetic regulation of gene expression, including histone acetylation and methylation [42]. Histone acetylation is frequently associated with gene activation, whereas methylation can lead to either activation or suppression of transcription [43]. Specific histone methylation has been observed under hypoxic conditions in various cell types [44]. Additionally, hypoxia in the tumor microenvironment appears to drive both hyperacetylation and hypermethylation in tumors. By analyzing the public ChIP-seq database, we found increased levels of H3K27ac and H3K4me3 acetylation and methylation markers, respectively, in the *GPCPD1* promoter region (Figure 2G). Our results also showed that H3K4me3 and H3K27ac gradually decreased around the promoter region of *GPCPD1* under hypoxic conditions after 72 h, which might impair the incremental persistence of *GPCPD1* expression by hypoxia after the turning point mentioned above.

Previous studies have demonstrated that *GPCPD1* has important functions in choline metabolism and contributes to cancer progression [18,45,46]. Subcellular localization of proteins is essential for cancer development and progression and is regulated by post-transcriptional modifications. Utilizing *in silico* prediction of protein-protein interactions, we detected an interaction between *GPCPD1* and LYPLA1, which are key players in the palmitoylation-depalmitoylation cycle [47], a reversible unique post-translational modification that modulates subcellular polarity and signaling cascade activity [48]. In particular, LYPLA1, but not LYPLA2, could exist in mitochondria with S-depalmitoylation activation, which was previously thought to reside in the cytosol and Golgi apparatus [32]. A recent study proposed that hypoxic conditions may initiate the oxidation of terminal cysteines, leading to depalmitoylation [49]. Our study revealed that *GPCPD1* has palmitoylated sites using bioinformatic prediction and proved that *GPCPD1* could be modified by palmitoylation using an acyl biotin exchange assay. During this process, subcellular trafficking of *GPCPD1* occurs, and *GPCPD1* is re-localized to the mitochondria. Therefore, we hypothesized that hypoxic conditions influenced depalmitoylation, which might remove palmitoyl-CoA from *GPCPD1* and then cluster it together to shuttle it from the membrane

(ML348) or siLYPLA1 respectively. (H) Immunofluorescence analysis of *GPCPD1* and VDAC1 in MDA468 cells with DMSO (control), 25  $\mu$ M palmB, or siLYPLA1 treatment respectively (under hypoxic conditions). Scale bar: 100  $\mu$ m. (I) Schematics showed *GPCPD1* contained two protein domains (CBM20 and GDPD\_GDE5). (J) Co-IP assays proved the interactions between *GPCPD1* and VDAC1 located in the CBM20 domain. (K) Conservation analysis for the *GPCPD1*-VDAC1 interaction site across different species and schematic of the mutant construct. (L) Co-IP assays showed the L257/L259 was the key site for the interaction between VDAC1 and *GPCPD1* in MDA468 cells.



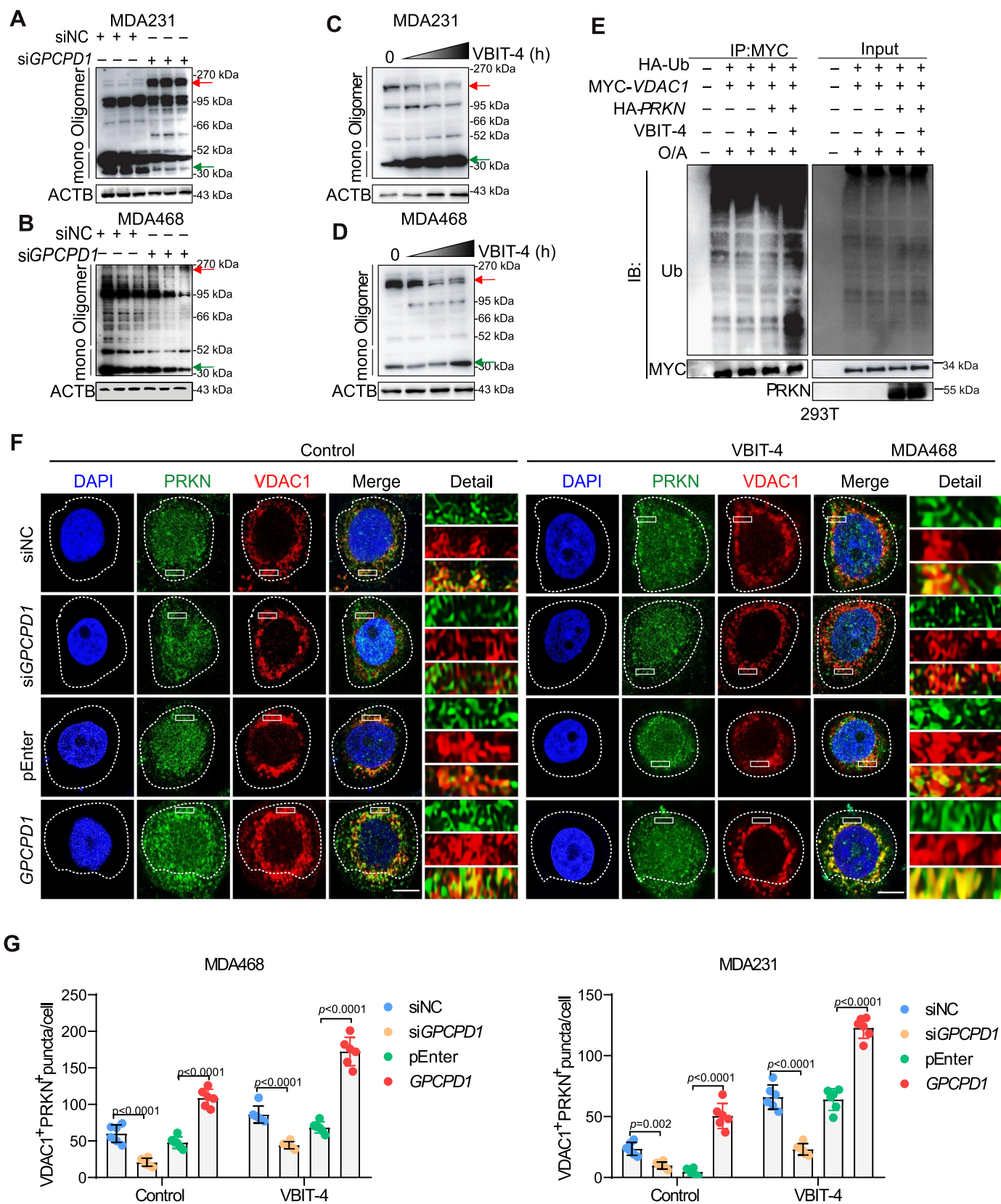


**Figure 6.** GPCPD1 promoted mitophagy by interfering with the oligomerization of VDAC1. (A and B) Oligomer and monomer of VDAC1 protein in MDA231 (A) and MDA468 (B) cells with *GPCPD1* knockdown. Oligomer, red arrows; monomer, green arrows. (C and D) Oligomer and monomer of VDAC1 protein in MDA231 (C) and MDA468 (D) cells after 10  $\mu$ M VBIT-4 agent treatment. (E) Co-IP and ubiquitination analyses of VDAC1 in 293 T cells after *PRKN* overexpression, with or without 20  $\mu$ M O/A or 10  $\mu$ M VBIT-4 treatment. (F and G) Immunofluorescence analysis of PRKN and VDAC1 in MDA468 cells after *GPCPD1* knockdown or overexpression with 10  $\mu$ M VBIT-4 treatment or not (under hypoxic conditions). Scale bar: 100  $\mu$ m. Statistical graphs (G) of yellow punctum in MDA231 and MDA468 cells (n = 6 representative cells).



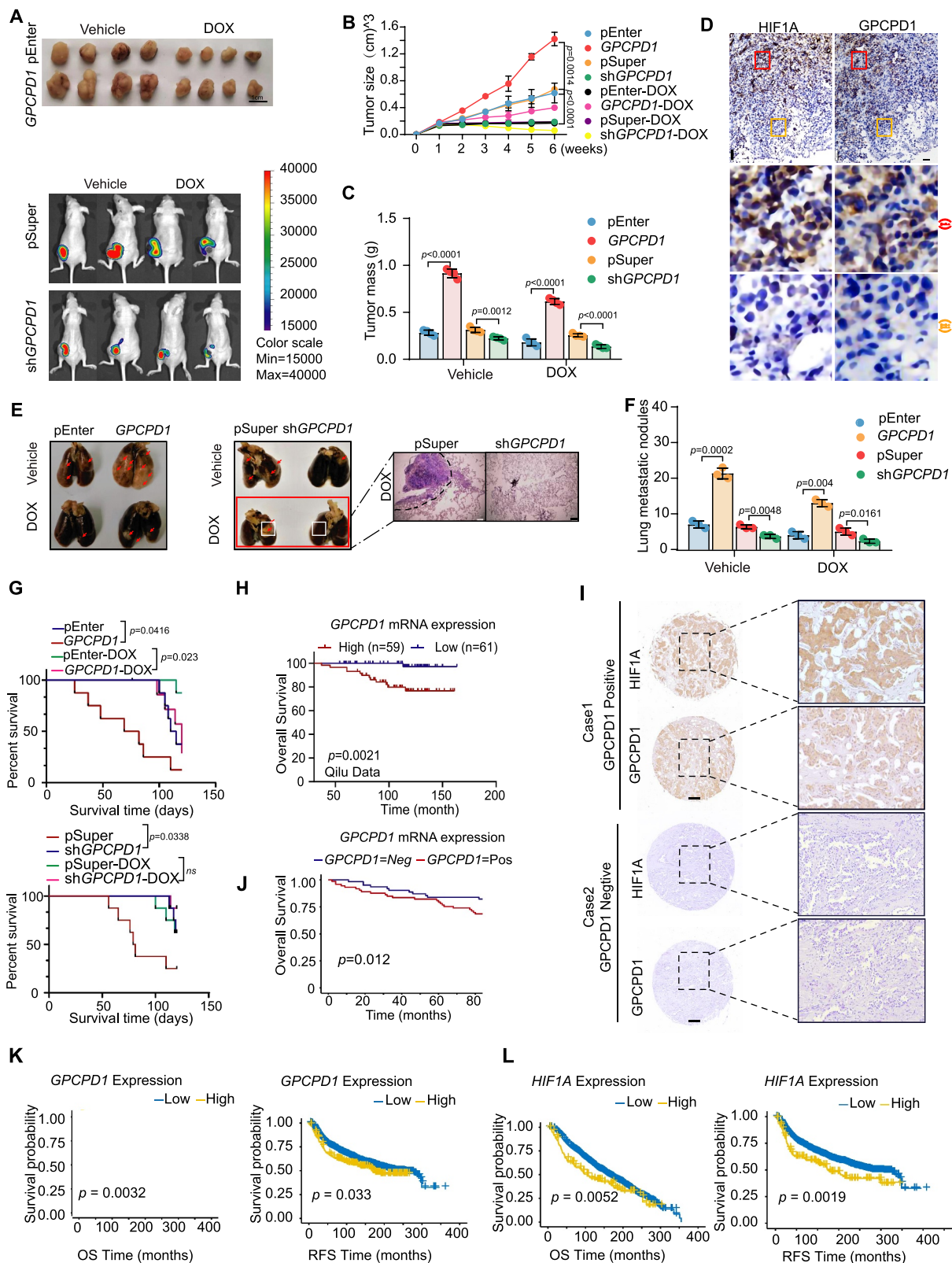


**Figure 7.** *GPCPD1* could serve as an independent prognostic marker in breast cancer. (A-D) Subcutaneous injection of MDA231 cells with *GPCPD1* overexpression or knockdown for tumor growth analysis ( $n = 4$  in each group). DOX (doxorubicin) was intravenously injected at 2 mg/kg, 3 times a week ( $n = 4$  in each group). Bioluminescent imaging (BLI) quantification and images of *GPCPD1* knockdown were shown at the bottom (A). Tumor growth curves (B) and tumor weight (C) were analyzed. *GPCPD1* and HIF1A staining in different areas of serial sections of xenografts was shown in (D). Red and yellow boxes indicated the areas with consistently high or low *GPCPD1*/HIF1A expressions respectively. Scale bar: 100  $\mu$ m. Higher magnifications of the marked areas were also displayed in panels (I) (red) and (ii) (yellow) respectively. (E-J) Intravenous injection of MDA231 cells with *GPCPD1* overexpression or knockdown for lung colonization analysis ( $n = 4$  in each group). Pulmonary surface nodules (E, left), hematoxylin and eosin (H&E) staining (E, right), and statistical diagram (F) in nude mice. Scale bar: 100  $\mu$ m. The survival analysis for (E). (H) Overall survival (OS) of patients with high or low *GPCPD1* mRNA expression based on the tissue from Qilu Hospital. (I) Representative immunohistochemistry images of *GPCPD1* and HIF1A protein expression in 329 human breast tumor tissues on the tissue microarrays. (J) OS of patients with high or low *GPCPD1* expression based on the tissue microarrays. (K and L) Kaplan-Meier survival analysis of OS and recurrence-free survival (RFS) in patients with high or low *GPCPD1* or *HIF1A* expression from the METABRIC database. (B, C, F) Two-tailed unpaired t-test. (G, H, J, K, L) Log-rank test.

or cytosol to the mitochondria. Our data are consistent with this assumption, which illustrated that GPCPD1 could be transported to mitochondria with depalmitoylation modification.

In our study, *GPCPD1* was shown to regulate mitophagy. However, how it plays a role in this process remains unclear. In our study, mass spectrometry and the co-IP assay validated that GPCPD1 could bind to the  $\beta$ -18 strand of VDAC1 in TNBC cells in hypoxic conditions, and we also found there is a weaker interaction between GPCPD1 and VDAC1 in normoxic conditions. VDAC1 is a transmembrane  $\beta$ -barrel pore protein that forms a variety of oligomeric forms through interactions with its component  $\beta$ -strands ( $\beta$ -1,  $\beta$ -17,  $\beta$ -18, and  $\beta$ -19) [36,50]. Recent studies have shown that VDAC1 oligomerization promotes CYCS/cytochrome c release during apoptosis, and VDAC1 oligomerization was strongly correlated with apoptosis induction [51,52]. In addition, recent studies have proposed that the interface of VDAC1 dimers involves amino acid residues located in  $\beta$ -strands 1 (Ile-27, Leu-29), 2 (Glu-50, Thr-51), 18 (Leu-257, Leu-259), and 19 (Leu-277) of both adjacent VDAC1 monomers [53,54]. We then demonstrated that the

downregulation of GPCPD1 could destroy VDAC1 oligomerization by directly binding to VDAC1. Additionally, mutation of these conserved sites (Leu-257 and Leu-259) of VDAC1 could partly disrupt the interaction with GPCPD1 (Figure 6(A AND b)). In general, our study indicates that GPCPD1 is relevant to the stability of VDAC1 oligomerization states. VDAC is expressed in the OMM, where it modulates metabolic and energy interchanges and is involved in mitophagy [55]. Furthermore, recent studies have shown that VDAC1 is indeed one of the regulators and plays an important role in mitophagy [56], and that reduced ubiquitination of VDAC1 inhibits PRKN recruitment, leading to a reduction in mitophagy [37]. It has also been reported that a VDAC1-hexokinase complex shields the oligomerization interface and prevents VDAC dimerization, which results in an anti-apoptotic response [57]. Consistently, we showed a relationship between VDAC1 oligomerization and PRKN-mediated VDAC1 polyubiquitination. Taken together, this is the first study to show that GPCPD1 contributes to the enrichment of the monomers of VDAC1, which facilitates the recruitment of PRKN-mediated polyubiquitination and consequently mitophagy.

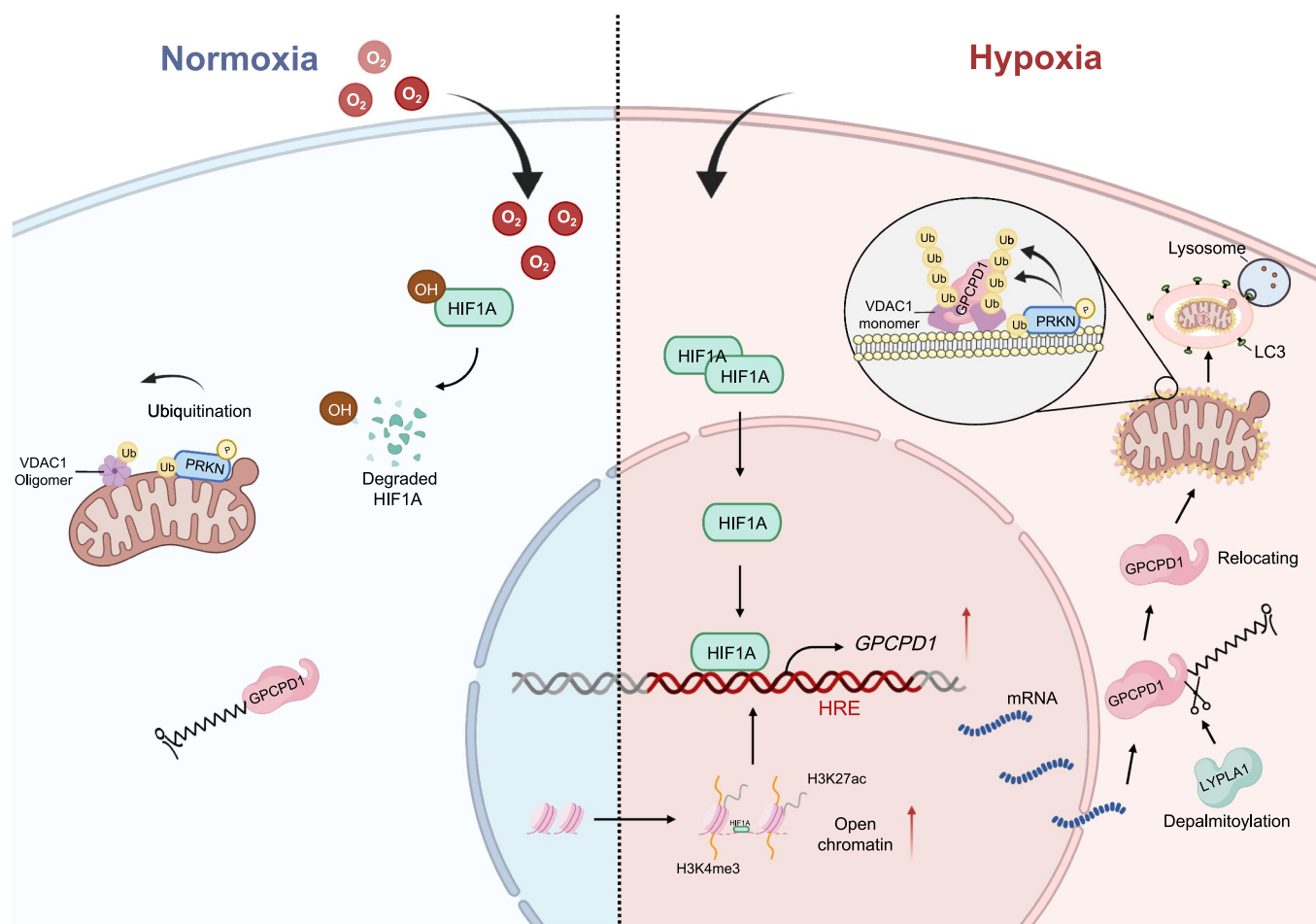


**Figure 8.** A schematic presentation of the role of GPCPD1 in hypoxia-induced mitophagy. Under hypoxia stress, *GPCPD1* was first transcriptionally regulated by HIF1A and histone modifications. After depalmitoylation by LYPLA1, GPCPD1 was trafficked to the outer mitochondria membrane, which facilitated the interaction between GPCPD1 and VDAC1. Then, GPCPD1 interfered with VDAC1 oligomerization, which activated the polyubiquitination mediated by PRKN and triggered mitophagy consequently.

## Conclusions

However, the role of *GPCPD1* in TNBC is poorly understood. For the first time, our study confirmed that *GPCPD1* as a HIF1A target gene regulates tumor growth and metastasis by mitophagy under hypoxic conditions. In addition, LYPLA1-mediated depalmitoylation contributes to *GPCPD1* localization to the OMM, and then *GPCPD1* interferes with the oligomerization of VDAC1, which recruits polyubiquitination mediated by PRKN. Taken together, our findings highlight the importance of *GPCPD1* as a mitophagy regulator in TNBC progression under hypoxic conditions (Figure 8).

## Materials and methods

### Cell culture and transfection

The TNBC cell lines MDA231 and MDA468 along with Human Embryonic Kidney (HEK) 293 T cells were bought via American Type Culture Collection (ATCC, HTB-26, HTB-132, and CRL-3216), which were cultured in DMEM/high glucose media (Hyclone, SH30157.01) enriched with 10% FBS (Gibco, 10099141C), 100 U/ml penicillin (Macgene, CC004), and 100 µg/ml streptomycin (Macgene, CC004). For normoxia, cells were cultured at 37°C with 5% CO<sub>2</sub> and 21% O<sub>2</sub>, and at 37°C with 5% CO<sub>2</sub> and 1% O<sub>2</sub> for hypoxia. Genetic Testing Biotechnology Corporation (Suzhou, China) used short tandem repeat (STR) markers to characterize the cell lines.

Cells were first transfected with the relative vectors for *GPCPD1* knockdown or overexpression. “pSuper” represented the control group that has been transfected with the pSuper vector in the knockdown experiment. Likewise, “pEnter” represented the control group that has been transfected with the pEnter vector in the overexpression experiment. The transfected cells were treated either with 2.5 µg/ml puromycin (Sigma-Aldrich, P9620) or 500 µg/ml G418 (Sigma-Aldrich, A1720) for 2 or 7 days respectively, to ensure stability. By employing Lipofectamine 2000 (Invitrogen, 11,668,019), separate siRNAs for *GPCPD1*, *VDAC1*, and *LYPLA1* (GenePharma, A09001) were transfected into the cells, according to the provided protocol. All the plasmids indicated in our study were constructed by ourselves and primers were shown in Table S6. The RNAi and shRNA sequences are listed in Table S6.

### Mt-Keima, MitoTracker detection, and reactive oxygen species (ROS) assay

For the mt-Keima detection, MDA231 and MDA468 cells were transfected with the MT-targeted mKeima-Red (mt-Keima; Amalgam, AM-V0251 HM) for 48 h. The fluorescence was measured by flow cytometry (BD Biosciences) after the resuspension of cells in phosphate-buffered saline (PBS; Solarbio, P1003). FlowJov10 software (Tree Star) was used to evaluate mitophagy. Visualization of mt-Keima was performed by excitation at 488 nm (for pH = 7) with 527/32 nm and 561 nm (for pH = 4) with 586/42 nm emission filters. For the MitoTracker detection, MDA231 and

MDA468 cells were incubated with the MitoTracker Deep Red (Thermo, M22426) for 30 min. The fluorescence images were examined using a confocal laser scanning microscope (ZEISS). ImageJ software was used for the processing and analysis of images. For the ROS assay, MDA231 and MDA468 cells were cultured in 6-cm plates and were washed three times with PBS, and 1 µM ROS probes (Thermo, C10422) were added. After that, the cells were incubated for 2 h at 37°C with or without hypoxia. The culture supernatant was then aspirated, and cells were rinsed twice with PBS. The FITC channel was utilized to filter the cells, and the FlowJov10 software was used to assess ROS levels.

### Immunofluorescence (IF) analysis

Cells were grown on coverslips in 24-well plates until 60% confluent after which they were fixed with 4% paraformaldehyde for 15 min followed by permeabilization for 30 min at room temperature. After blocking (3% BSA [Solarbio, A8010], 1 h, room temperature), and after a night of incubation at 4°C with the primary antibody, the cells were treated for 1 hour at room temperature with fluorescent-labeled secondary antibodies. After counterstaining the nuclei with DAPI (Roche) for 30 min, cells were mounted and examined using a confocal laser scanning microscope (ZEISS). ImageJ software was used for the processing and analysis of images.

### RNA-Sequencing and analysis of data

Total RNA from MDA231 and MDA468 with indicated treatments (1% O<sub>2</sub> or carbonyl cyanide m-chlorophenyl hydrazone [CCCP; Sigma-Aldrich, C2759]) were extracted with TRIzol reagent (Invitrogen, 15,596,018). Then all the RNA-sequencing was performed by Novogene Company (Tianjin, China). The raw reads were aligned to hg38 using STAR (v2.4.2a) with the “quantMode” parameter set as “GeneCounts”, resulting in count tables for the genes. The “DEseq2” package in R (v3.18.1) was used to identify differentially expressed genes. The read count tables were filtered to retain genes having a minimum of counts across all conditions. All RNA-sequencing original data have been uploaded to Sequence Read Archive (SRA) database with the number PRJNA742841 (<https://www.ncbi.nlm.nih.gov/bioproject/?term=GPCPD1>).

### Quantitative real-time PCR (qPCR)

Total RNA was extracted as above and reverse-transcribed to cDNA, which was then analyzed by qPCR using FastStart Universal SYBR Green Master (Takara, RR430A), following the provided protocol. The Light Cycler 480 Real-Time PCR machine (Roche) was employed to perform the amplification as follows: 95°C for 10 min, followed by 40 cycles of 95°C for 15s, 59°C for 30s, and 70°C for 30s, followed by a melting curve analysis to validate primer specificity. Samples were run in triplicate (three technical replicates) with the cycle threshold (CT) values normalized to *ACTB* for comparison with control samples.



### Dual-luciferase reporter assay

HEK293T cells were grown in 96-well plates and were transfected with the indicated firefly luciferase reporter plasmids for 36 h. After removing half of the culture supernatant (leaving 50  $\mu$ L in each well), 50  $\mu$ L luciferase firefly buffer (25 mM glycylglycine [Promega, E194A], 15 mM potassium phosphate, 15 mM  $MgSO_4$ , 2 mM ATP [Promega, E195A], 10 mM DTT, and 1 mM D-luciferin [Promega, E151A], pH 7.8) were added and incubated for 15 min at room temperature. Luminescence was measured immediately using a Multimode Plate Reader (PerkinElmer). Then we added 50  $\mu$ L Renilla buffer (0.5 M NaCl, 1 mM EDTA, 0.1 M potassium phosphate, 0.04% BSA, and 2  $\mu$ M coelenterazine [Promega, E640A, and E641A], pH 7.4) for 15 min at room temperature and detected luminescence in the same way.

### Chromatin immunoprecipitation (ChIP)

ChIP assays were conducted with an EZ-ChIP Kit (Millipore, 17-371), following the manufacturer's instructions. Briefly, MDA468 cells were cross-linked using 1% formaldehyde for 10 min at room temperature, followed by quenching in 0.125 M glycine for 5 min. Cells were harvested in SDS lysis buffer and the DNA was fragmented into 200–1000-bp fragments by sonication. After pre-clearing, samples were incubated with the primary or control IgG antibodies overnight and then incubated with protein-A/G agarose beads (Millipore, IP05) for 2 h at 4°C. After washing, the chromatin was eluted from the beads using TES buffer (1% SDS, 1 mM EDTA, 10 mM Tris-Cl, pH 8.0) and incubated with proteinase K (Millipore, 20-298) at 55°C for 45 min followed by overnight incubation at 65°C. The DNA was extracted with phenol-chloroform, precipitated with ethanol, and analyzed by qPCR. Fold enrichment was in comparison with IgG. The primers used are shown in Table S6.

### Cell viability and colony formation assays

For measuring cell viability, MDA231, and MDA468 cells were cultured in 96-well plates. MTT (Sigma Aldrich, M2003) was incubated with the cells for 6 h at 37°C. Then the supernatant was discarded, and the precipitate was dissolved in DMSO. Absorbances at 490 nm were measured in a microplate reader. To examine colony formation, cells were plated in 6-well plates with a replacement of the medium every four days for four weeks. When the colonies were visible, they were stained and counted.

### Migration and invasion assays

MDA231 and MDA468 cells were seeded into Transwell inserts (Corning, 353,097) at a concentration of  $8 \times 10^4$  cells/well, and 20% FBS was added to the bottom of the 24-well plates. After 24 h, the cells on the lower surface of the membrane were stained with 0.1% crystal violet. A minimum of three fields were imaged and counted using Image-Pro Plus6.0 software. The invasion assay was conducted similarly

apart from coating the membrane with 15% Matrigel (Corning, 354,234) in DMEM.

### EdU staining

For EdU staining, MDA231 and MDA468 cells in 96-well plates were incubated with EdU buffer A from the EdU Imaging Kit (RIBOBIO, C10310-1) for 2 h, followed by fixing with 4% paraformaldehyde for 30 min. Next, 2 mg/ml glycine was added and cells were rinsed with three washes of PBS. The cells were permeabilized with 0.4% Triton X-100 (Thermo, 85,111) for 10 min at room temperature, and the cells were stained with 1 $\times$  Apollo solution for 30 min in the dark and then washed. After nuclear staining with 1 $\times$  Hoechst 33,342 for 30 min, followed by washing, the cells were observed and imaged with a confocal laser scanning microscope (ZEISS) and images were analyzed with ImageJ.

### Mitochondrial membrane potential detection assay

MDA231 and MDA468 cells were grown in 96-well plates. After washing, the cells were stained in 50  $\mu$ L DMEM and 50  $\mu$ L JC-1 (Thermo, M34152) solution for 20 min at 37°C. This was followed by two washes with JC-1 solution and the addition of DMEM to the wells. The presence of the JC-1 was assessed with excitation and emission wavelengths of 490 and 530 nm, respectively, followed by an assessment of the JC-1 polymer at excitation and emission wavelengths of 525 and 590 nm, respectively, using the microplate reader.

### Oxygen consumption measurement

MDA231 and MDA468 cells with *GPCPD1* overexpression or knockdown were seeded in XF96-well plates (25,000 per well), and then grown at 37°C overnight. The medium was then replaced with XF Assay Medium (Agilent, 103,575-100) containing 10 mM glucose, 1 mM pyruvate (Agilent, 103,577-100 and 103,578-100), and 2 mM glutamine (Agilent, 103,579-100) for 1 h at 37°C. Oxygen consumption rates (OCR) were determined using the Seahorse XF mitochondrial stress test (Agilent). Briefly, injection ports were loaded to achieve the following final working concentrations in MDA231 and MDA468 cells: oligomycin (0.5  $\mu$ M; Agilent, 103,015-100), FCCP (1  $\mu$ M; Agilent, 103,015-100), rotenone (1  $\mu$ M; Agilent, 103,015-100), and antimycin A (1  $\mu$ M; Agilent, 103,015-100). Data were analyzed using Wave software calculating the basal respiration (minimum rate measurement after rotenone+antimycin A injection) and spare respiratory capacity (maximum rate measurement after FCCP injection subtract the non-mitochondrial respiration rate).

### Western blotting

After harvesting and washing the cells, the protein was extracted in RIPA lysis buffer (50 mM Tris, pH 8.0, 150 mM NaCl, 1% Triton X-100, 0.5% sodium deoxycholate [Millipore, 20,188], 0.1% SDS, and 1 mM phenylmethylsulfonyl fluoride [PMSF; Beyotime, ST506]) and concentrations determined with a BCA kit (Millipore, 71,285). Proteins were separated

on SDS-PAGE and transferred to PVDF membranes (Millipore, ISEQ00010). After blocking with 5% BSA in TBS (Solarbio, A8010) containing 0.1% Tween 20 (Thermo, 85,113), the blots were probed with primary and HRP-conjugated secondary antibodies (Abcam, ab205718), followed by visualization using an ECL kit (Bio-Rad, 1,705,060). The following antibodies were used: Rabbit anti-GPCPD1 (HPA039556) was obtained from Sigma-Aldrich. Mouse anti-GPCPD1 (PA5-65,346, Immunofluorescence) was obtained from Invitrogen. Rabbit anti-HIF1A (36,169), rabbit anti-H3K27ac (8173), rabbit anti-H3K4Me3 (9751), mouse anti-ubiquitin (3936), and rabbit anti-MT-CO2/COX2 (31,219) were obtained from Cell Signaling Technology. Rabbit anti-FUNDC1 (YT5658) and rabbit anti-LYPLA2 (YN0404) were obtained from ImmunoWay Biotechnology. Rabbit anti-Flag (07-1586) was obtained from EMD Millipore. Rabbit anti-HSPD1 (15,282-1-AP), rabbit anti-VDAC1 (55,259-1-AP), mouse anti-TOMM20 (66,777-1-Ig), rabbit anti-PINK1 (23,274-1-AP), rabbit anti-PRKN (14,060-1-AP), rabbit anti-LC3B (14,600-1-AP), rabbit anti-BNIP3L (12,986-1-AP), mouse anti-BNIP3 (68,091-1-Ig), rabbit anti-LYPLA1 (16,055-1-AP), rabbit anti-Flag (20,543-1-AP), mouse anti-ACTB (66,009-1-Ig), rabbit anti-MKI67 (27,309-1-AP), mouse anti-MYC (60,003-2-Ig), rabbit anti-MFN1 (13,798-1-AP), mouse anti-MFN2 (67,487-1-Ig), rabbit anti-FIS1 (10,956-1-AP), rabbit anti-MT-CYB (55,090-1-AP), and rabbit anti-MT-ND2 (19,704-1-AP) were obtained from Proteintech.

### Co-immunoprecipitation (co-IP)

After transfection with overexpression plasmids for 48 h, cells were lysed in IP lysis buffer (Beyotime, P0013) for 30 min. Next, 3 µg immunoprecipitating primary antibody or control IgG was added to protein samples (500 µg) with gentle rotation for 2 h at 4°C. After an overnight (4°C) incubation with 40 µl protein-A/G agarose (Santa Cruz Biotechnology, sc-2003), the beads were washed four times with IP lysis buffer, followed by resuspension in 40 µl 2 × SDS sample buffer with heating at 95°C for 10 min. The samples were evaluated by immunoblotting.

### Ubiquitination analysis

After transfection of HEK293T cells with HA-*Ub*, MYC-*VDAC1*, and 3× HA-*PRKN* by using Lipofectamine 3000 (Invitrogen, L30000015), the cells were treated with VBIT-4 (VDAC inhibitor; SELLECK, S3544) or O/A (oligomycin A, SELLECK, S1478; and antimycin, Santa Cruz Biotechnology, sc-202,467; 1:1) and lysed with IP lysis buffer for 30 min, followed by co-immunoprecipitation as described above. The degree of ubiquitination was assessed by immunoblotting with an anti-ubiquitination mouse polyclonal antibody.

### Protein mass spectrometry

MDA468 cells with Flag-*GPCPD1* overexpression and control cells with pCMV-Flag overexpression under hypoxic treatment or not for 48 h were collected with IP lysis buffer plus protease

inhibitor (Millipore, 20,188). Then 3 µg antibodies (anti-GPCPD1 or anti-IgG) were added to the protein samples (500 µg) and incubated with gentle rotation for 2 h at 4°C. The proteins were then incubated with 40 µl protein-A/G agarose overnight at 4°C followed by lysis in MS buffer (50 mM HEPES, pH 7.0, 100 mM KCl, 0.5% NP-40 [Sigma-Aldrich, NP40S], 2 mM EDTA, 10% glycerol [Sigma-Aldrich, G2025]). LC-MS/MS was conducted and evaluated by PTM Biolabs (Hangzhou, China). The LC-MS results are shown in Table S7.

### Nucleocytoplasmic separation

Nucleocytoplasmic separation was conducted with a cell nucleocytoplasmic separation kit (Thermo, 78,833) following the provided directions. Treated cells ( $1 \times 10^7$ ) were harvested and gently resuspended in ice-cold cytosol extraction buffer (20 mM potassium-HEPES, pH 7.4, 10 mM KCl, 1.5 mM MgCl<sub>2</sub>, 250 mM sucrose [Thermo, 78833A], 1 mM Na-EDTA, 1 mM DTT and 0.1 µM PMSF) and placed on ice for 1 min. After centrifugation (12,000 g; 5 min, 4°C), the supernatants containing the cytoplasmic extracts were placed in clean pre-chilled tubes. The pellets containing the nuclei were resuspended in a 200 µL ice-cold nuclei lysis buffer, vortexed, and placed on ice for 1 min. After further centrifugation (14,000 g; 10 min; 4°C), the nucleoplasmic extracts in the supernatants were stored at -80°C.

### Mitochondrial isolation

Mitochondria were isolated using a kit (Thermo, 89,874) and differential centrifugation. Treated cells ( $1 \times 10^7$ ) were centrifuged (300 g; 10 min; 4°C) and rinsed in PBS, followed by incubation with 1 ml mitochondrial isolation reagent for 15 min on ice. Cells were transferred to a glass vial and stained with trypan blue after being homogenized 35 times. After centrifugation (600 g; 10 min; 4°C), transfer of the supernatant to a clean tube, and re-centrifugation (11,000 g; 10 min; 4°C), the pellet containing the mitochondria was lysed in mitochondria lysis solution and the protein content measured by BCA. In addition, the supernatant above was centrifuged (12,000 g; 10 min; 4°C) and the whole-cell protein supernatant without the mitochondria was collected and measured by BCA.

### Acyl biotin exchange (ABE) assay

This was conducted using a published protocol [58]. MDA468 cells ( $1 \times 10^7$ ) were transfected with Flag-*GPCPD1*. After 48 hours, cells were lysed in 1 ml lysis buffer (50 mM Tris-HCl, pH 7.4, 150 mM NaCl, and 5 mM EDTA containing EDTA-free protease inhibitor [Millipore, 20,188]) with 10 mM N-ethylmaleimide (NEM; Sigma-Aldrich, E1271). And then cells were incubated with rotation for 30 min at 4°C. Next, the cell lysate was collected in a 1.5 ml tube by centrifugation at 16,000 g for 30 min. Then 5 µg Flag antibody was added to each tube with 400 µl cell lysate and the antibody-lysate mixture was rotated overnight at 4°C. Sixty microliters of protein A/G beads were added to each of the antibody-

lysate mixtures with rotation for 2 h at 4°C. The samples were rinsed with LB (pH 7.2) and the beads were resuspended in 600 µl LB with 10 mM NEM for 10 min on ice. Afterward, each sample was split into +HAM group and -HAM group by adding hydroxylamine (HAM; Sigma-Aldrich, 438,227) or not, and then -HAM samples and +HAM samples were added to 0.5 ml/sample of LB pH 7.2 or 1 M HAM buffer respectively. Samples were incubated for 1 h at room temperature, followed by washing with LB (pH 6.2) and collection of the pelleted beads on ice. Then, 0.5 ml of 2.5 µM Biotin-BMCC buffer (Thermo, 21,900; LB pH 6.2 as the solution) was added to each sample and allowed to incubate for exactly 1 h at 4°C. After another wash with LB (pH 6.2), the beads were collected and a 2× SDS sample buffer was added to each sample to achieve a final concentration of 5 mM. Samples were boiled for 10 min at 75–80°C, separated, and immunoblotted.

### Immunohistochemistry (IHC)

IHC was conducted using a ZSGB-BIO kit (ZSGB-BIO, SP9000) according to provided directions. After dewaxing and antigen retrieval in sodium citrate buffer, the sections were blocked and incubated with primary antibodies against GPCPD1, MKI67, or HIF1A at 4°C overnight. After incubation with the secondary antibody, the proteins were visualized with 3,3-N-diaminobenzidine tetrahydrochloride (DAB; ZSGB-BIO, ZLI-9017) and assessed in a blinded manner by two pathologists using a semi-quantitative method and scored as negative (0), weak (1), moderate (2), or strong (3) in terms of staining intensity and percentages of cytoplasmic and nuclear staining.

### Mouse experiments

All animal studies were conducted according to the guidelines for the care and use of laboratory animals, which were approved by the Institutional Biomedical Research Ethics Committee of the Qilu Hospital of Shandong University. Two hundred microliters of MDA231 or MDA231-Luc cells ( $1 \times 10^7$ ) with *GPCPD1* stable overexpression or knockdown in PBS were injected subcutaneously into the flanks of 4-6-week-old female BALB/C athymic nude mice. The tumors were measured weekly with calipers or monitored with a noninvasive bioluminescence system, and the volumes were determined by the length  $\times$  width<sup>2</sup> / 2. On day 14, the mice were treated via intravenous injection with 2 mg/kg doxorubicin (Sigma-Aldrich, D1515) or PBS (vehicle) three times a week. For lung metastasis assays,  $1 \times 10^5$  cells were resuspended in 100 µl PBS, and cells were intravenously injected into 6-week-old female BALB/c nu/nu mice. On day 8 post-injection, the mice were treated via intravenous injection with 2 mg/kg doxorubicin or PBS (vehicle) three times a week. Mice were sacrificed when moribund. The tumors and lungs were fixed in formalin and embedded in paraffin.

### Clinical sample analysis

The Institutional Research Ethics Committee of Qilu Hospital of Shandong University provided the approval for the study. Human breast cancer tissue microarrays (TMAs) were obtained from Outdo Biotech (HBre-Duc1405ur). Clinical samples were collected at Qilu Hospital of Shandong University and all participants provided informed consent voluntarily. For the Kaplan–Meier survival analysis, samples were divided into low- (scores 0 and 1) and high- (scores 2 and 3) expression groups for GPCPD1 and HIF1A. Multivariate Cox analysis was conducted to evaluate the hazard ratio (HR) of GPCPD1 expression and the clinicopathological parameters.

### Statistical analysis

The sample sizes and tests used in each experiment are shown in the figure legends. Data analysis and graphics were done with GraphPad Prism 8 and R. *P*-values <0.05 were considered significant; precise *p*-values are given in the figures.

### Disclosure statement

No potential conflict of interest was reported by the authors.

### Funding

This work was supported by the National Key Research and Development Program of China [2020YFA0712400]; National Natural Science Foundation of China [No. 81972475]; National Natural Science Foundation of China [No. 81874119; No. 82072912]; Qilu Hospital Clinical New Technology Developing Foundation [No. 2018-7; No. 2019-3]; The Key Research and Development Program of Shandong Province [2019GSF108140]; Chinese Postdoctoral Science Foundation [2019T120593; 2018M630787]; Special Foundation for Taishan Scholars [No. ts20190971]; Special Support Plan for National High-Level Talents [W01020103]; Foundation from Clinical Research Center of Shandong University [No.2020SDUCRCA015].

### Ethics approval and consent to participate

Shandong University Qilu Hospital's Ethics Committee for Scientific Research provided the approvals for all the animal tests that were carried out and for the protocol according to which the participants were included in the study. Before the start of the study, all participants voluntarily provided their Informed consent forms. The approval number is KYLL-2019(KS)-113 and KYLL-2016-255 respectively.

### Consent for publication

All authors agreed on the manuscript.

### Data availability statement

The data generated in this study are available within the article.

### ORCID

Ying Liu  <http://orcid.org/0000-0001-9216-0009>  
 Hanwen Zhang  <http://orcid.org/0000-0003-4973-0242>  
 Yiwei Liu  <http://orcid.org/0000-0001-9885-6429>  
 Siyue Zhang  <http://orcid.org/0000-0003-2723-9428>



Peng Su <http://orcid.org/0000-0002-7000-0474>  
 Lijuan Wang <http://orcid.org/0000-0002-7885-9945>  
 Yaming Li <http://orcid.org/0000-0001-5627-229X>  
 Yiran Liang <http://orcid.org/0000-0002-2404-0408>  
 Xiaolong Wang <http://orcid.org/0000-0002-4971-4835>  
 Weijing Zhao <http://orcid.org/0000-0003-4477-596X>  
 Bing Chen <http://orcid.org/0000-0003-0168-8532>  
 Dan Luo <http://orcid.org/0000-0003-2250-8705>  
 Ning Zhang <http://orcid.org/0000-0002-6430-4236>  
 Qifeng Yang <http://orcid.org/0000-0003-0576-8513>

## References

- [1] Williams AS, Koves TR, Davidson MT, et al. Disruption of acetyl-lysine turnover in muscle mitochondria promotes insulin resistance and redox stress without overt respiratory dysfunction. *Cell Metab.* 2020;31(1):131–147. e11.
- [2] Wu H, Chen Q. Hypoxia activation of mitophagy and its role in disease pathogenesis. *Antioxid Redox Signal.* 2015;22(12):1032–1046.
- [3] Zhang W, Siraj S, Zhang R, et al. Mitophagy receptor FUNDC1 regulates mitochondrial homeostasis and protects the heart from I/R injury. *Autophagy.* 2017;13(6):1080–1081.
- [4] Onishi M, Yamano K, Sato M, et al. Molecular mechanisms and physiological functions of mitophagy. *EMBO J.* 2021;40(3):e104705.
- [5] Drake LE, Springer MZ, Poole LP, et al. Expanding perspectives on the significance of mitophagy in cancer. *Semin Cancer Biol.* 2017;47:110–124.
- [6] Liu L, Feng D, Chen G, et al. Mitochondrial outer-membrane protein FUNDC1 mediates hypoxia-induced mitophagy in mammalian cells. *Nat Cell Biol.* 2012;14(2):177–185.
- [7] Chen Z, Siraj S, Liu L, et al. MARCH5-FUNDC1 axis fine-tunes hypoxia-induced mitophagy. *Autophagy.* 2017;13(7):1244–1245.
- [8] Abou Khouzam R, Goutham HV, Zaarour RF, et al. Integrating tumor hypoxic stress in novel and more adaptable strategies for cancer immunotherapy. *Semin Cancer Biol.* 2020;65:140–154.
- [9] Wu H, Wang T, Liu Y, et al. Mitophagy promotes sorafenib resistance through hypoxia-inducible ATAD3A dependent Axis. *J Exp Clin Cancer Res.* 2020;39(1):274.
- [10] Dowling CM, Hollinshead KER, Di Grande A, et al. Multiple screening approaches reveal HDAC6 as a novel regulator of glycolytic metabolism in triple-negative breast cancer. *Sci Adv.* 2021;7(3):eabc4897.
- [11] Stover DG, Parsons HA, Ha G, et al. Association of cell-free DNA tumor fraction and somatic copy number alterations with survival in metastatic triple-negative breast cancer. *J Clin Oncol.* 2018;36(6):543–553.
- [12] Abu-Jamous B, Buffa FM, Harris AL, et al. In vitro downregulated hypoxia transcriptome is associated with poor prognosis in breast cancer. *Mol Cancer.* 2017;16(1):105.
- [13] Loibl S, Poortmans P, Morrow M, et al. Breast cancer. *Lancet.* 2021;397(10286):1750–1769.
- [14] Ma Z, Xiang X, Li S, et al. Targeting hypoxia-inducible factor-1, for cancer treatment: recent advances in developing small-molecule inhibitors from natural compounds. London: *Semin Cancer Biol.* 2020.
- [15] Huang T, Xu T, Wang Y, et al. Cannabidiol inhibits human glioma by induction of lethal mitophagy through activating TRPV4. *Autophagy.* 2021;17(11):3592–3606.
- [16] Tamada H, Kiryu-SEO S, Hosokawa H, et al. Three-dimensional analysis of somatic mitochondrial dynamics in fission-deficient injured motor neurons using FIB/SEM. *J Comp Neurol.* 2017;525(11):2535–2548.
- [17] Lesjak MS, Marchan R, Stewart JD, et al. EDI3 links choline metabolism to integrin expression, cell adhesion and spreading. *Cell Adh Migr.* 2014;8(5):499–508.
- [18] Stewart JD, Marchan R, Lesjak MS, et al. Choline-releasing glycerophosphodiesterase EDI3 drives tumor cell migration and metastasis. *Proc Natl Acad Sci U S A.* 2012;109(21):8155–8160.
- [19] Adriaens ME, Prickaerts P, Chan-Seng-Yue M, et al. Quantitative analysis of ChIP-seq data uncovers dynamic and sustained H3K4me3 and H3K27me3 modulation in cancer cells under hypoxia. *Epigenetics Chromatin.* 2016;9:48.
- [20] Kwak YT, Muralimanoharan S, Gogate AA, et al. Human trophoblast differentiation is associated with profound gene regulatory and epigenetic changes. *Endocrinology.* 2019;160(9):2189–2203.
- [21] Kim YS, Nam HJ, Han CY, et al. Liver X receptor alpha activation inhibits autophagy and lipophagy in hepatocytes by dysregulating autophagy-related 4B cysteine peptidase and Rab-8B, reducing mitochondrial fuel oxidation. *Hepatology.* 2021;73(4):1307–1326.
- [22] Choudhry H, Harris AL. Advances in hypoxia-inducible factor biology. *Cell Metab.* 2018;27(2):281–298.
- [23] Schmaltz C, Hardenbergh PH, Wells A, et al. Regulation of proliferation-survival decisions during tumor cell hypoxia. *Mol Cell Biol.* 1998;18(5):2845–2854.
- [24] Xue M, Chen W, Xiang A, et al. Hypoxic exosomes facilitate bladder tumor growth and development through transferring long non-coding RNA-UCA1. *Mol Cancer.* 2017;16(1):143.
- [25] Xie Y, Lin H, Wei W, et al. LINC00839 promotes malignancy of liver cancer via binding FMNL2 under hypoxia. *Sci Rep.* 2022;12(1):18757.
- [26] Chen S, Chen J, Shi H, et al. *Abstract MP265: the role of phosphodiesterase 10a in tumor growth and doxorubicin-induced cardiotoxicity.* *Circ Res.* 2021;129(Suppl\_1):AMP265.
- [27] Santel A, Fuller MT. Control of mitochondrial morphology by a human mitofusin. *J Cell Sci.* 2001;114(Pt 5):867–874.
- [28] Hermann GJ, Thatcher JW, Mills JP, et al. Mitochondrial fusion in yeast requires the transmembrane GTPase Fzo1p. *J Cell Biol.* 1998;143(2):359–373.
- [29] Amendola CR, Mahaffey JP, Parker SJ, et al. KRAS4A directly regulates hexokinase I. *Nature.* 2019;576(7787):482–486.
- [30] Chan P, Han X, Zheng B, et al. Autopalmitoylation of TEAD proteins regulates transcriptional output of the Hippo pathway. *Nat Chem Biol.* 2016;12(4):282–289.
- [31] Zhao L, Zhang C, Luo X, et al. CD36 palmitoylation disrupts free fatty acid metabolism and promotes tissue inflammation in non-alcoholic steatohepatitis. *J Hepatol.* 2018;69(3):705–717.
- [32] Kathayat RS, Cao Y, Elvira PD, et al. Active and dynamic mitochondrial S-depalmitoylation revealed by targeted fluorescent probes. *Nat Commun.* 2018;9(1):334.
- [33] Camara AKS, Zhou Y, Wen PC, et al. Mitochondrial VDAC1: a key gatekeeper as potential therapeutic target. *Front Physiol.* 2017;8:460.
- [34] Nasr ML, Baptista D, Strauss M, et al. Covalently circularized nanodiscs for studying membrane proteins and viral entry. *Nat Methods.* 2017;14(1):49–52.
- [35] Bayrhuber M, Meins T, Habeck M, et al. Structure of the human voltage-dependent anion channel. *Proc Natl Acad Sci U S A.* 2008;105(40):15370–15375.
- [36] Najbauer EE, Tekwani Movellan K, Giller K, et al. Structure and gating behavior of the human integral membrane protein VDAC1 in a lipid bilayer. *J Am Chem Soc.* 2022;144(7):2953–2967.
- [37] Ham SJ, Lee D, Yoo H, et al. Decision between mitophagy and apoptosis by Parkin via VDAC1 ubiquitination. *Proc Natl Acad Sci U S A.* 2020;117(8):4281–4291.
- [38] Xia J, Chu C, Li W, et al. Mitochondrial protein UCP1 inhibits the malignant behaviors of triple-negative breast cancer through activation of mitophagy and pyroptosis. *Int J Biol Sci.* 2022;18(7):2949–2961.
- [39] Palikaras K, Daskalaki I, Markaki M, et al. Mitophagy and age-related pathologies: development of new therapeutics by targeting mitochondrial turnover. *Pharmacol Ther.* 2017;178:157–174.
- [40] Chourasia AH, Boland ML, Macleod KF. Mitophagy and cancer. *Cell Metab.* 2015;3:4.

- [41] Singleton DC, Rouhi P, Zois CE, et al. Hypoxic regulation of RIOK3 is a major mechanism for cancer cell invasion and metastasis. *Oncogene*. 2015;34(36):4713–4722.
- [42] Richart L, Picod-Chedotel ML, Wassef M, et al. XIIST loss impairs mammary stem cell differentiation and increases tumorigenicity through Mediator hyperactivation. *Cell*. 2022;185(12):2164–2183.e25.
- [43] Dawson MA. The cancer epigenome: concepts, challenges, and therapeutic opportunities. *Science*. 2017;355(6330):1147–1152.
- [44] Batie M, Frost J, Frost M, et al. Hypoxia induces rapid changes to histone methylation and reprograms chromatin. *Science*. 2019;363(6432):1222–1226.
- [45] Marchan R, Buttner B, Lambert J, et al. Glycerol-3-phosphate acyltransferase 1 promotes tumor cell migration and poor survival in ovarian carcinoma. *Cancer Res*. 2017;77(17):4589–4601.
- [46] Abeykoon JP, Wu X, Nowakowski KE, et al. Salicylates enhance CRM1 inhibitor antitumor activity by induction of S-phase arrest and impairment of DNA-damage repair. *Blood*. 2021;137(4):513–523.
- [47] Azizi SA, Kathayat RS, Dickinson BC. Activity-based sensing of S-depalmitoylases: chemical technologies and biological discovery. *Acc Chem Res*. 2019;52(11):3029–3038.
- [48] Wang W, Runkle KB, Terkowski SM, et al. Protein depalmitoylation is induced by wnt5a and promotes polarized cell behavior. *J Biol Chem*. 2015;290(25):15707–15716.
- [49] Goloshvili G, Barbakadze T, Mikeladze D. Sodium nitroprusside induces H-Ras depalmitoylation and alters the cellular response to hypoxia in differentiated and undifferentiated PC12 cells. *Cell Biochem Funct*. 2019;37(7):545–552.
- [50] Karmi O, Marjault HB, Bai F, et al. A VDAC1-mediated NEET protein chain transfers [2Fe-2S] clusters between the mitochondria and the cytosol and impacts mitochondrial dynamics. *Proc Natl Acad Sci U S A*. 2022;119(7): e2121491119.
- [51] Hu Q, Zhang H, Gutierrez Cortes N, et al. Increased Drp1 acetylation by lipid overload induces cardiomyocyte death and heart dysfunction. *Circ Res*. 2020;126(4):456–470.
- [52] Seo JH, Chae YC, Kossenkov AV, et al. MFF regulation of mitochondrial cell death is a therapeutic target in cancer. *Cancer Res*. 2019;79(24):6215–6226.
- [53] Ujwal R, Cascio D, Chaptal V, et al. Crystal packing analysis of murine VDAC1 crystals in a lipidic environment reveals novel insights on oligomerization and orientation. *Channels (Austin)*. 2009;3(3):167–170.
- [54] Kim J, Gupta R, Blanco LP, et al. VDAC oligomers form mitochondrial pores to release mtDNA fragments and promote lupus-like disease. *Science*. 2019;366(6472):1531–1536.
- [55] Shoshan-Barmatz V, Shteinifer-Kuzmine A, Verma A. *VDAC1 at the intersection of cell metabolism, apoptosis, and diseases*. *Biomolecules*. 2020;10(11):1485.
- [56] Ordureau A, Paulo JA, Zhang W, et al. Dynamics of PARKIN-dependent mitochondrial ubiquitylation in induced neurons and model systems revealed by digital snapshot proteomics. *Mol Cell*. 2018;70(2):211–227. e8
- [57] Ben-Hail D, Begas-Shvartz R, Shalev M, et al. Novel compounds targeting the mitochondrial protein VDAC1 inhibit apoptosis and protect against mitochondrial dysfunction. *J Biol Chem*. 2016;291(48):24986–25003.
- [58] Brigidi GS, Bamji SX. Detection of protein palmitoylation in cultured hippocampal neurons by immunoprecipitation and acyl-biotin exchange (ABE). *J Vis Exp*. 2013;(72):50031.